

Measurement of anti- ^3He nuclei absorption in matter and impact on their propagation in the Galaxy

(ALICE Collaboration) Acharya, S.; ...; Erhardt, Filip; ...; Gotovac, Sven; ...; Jerčić, Marko; ...; Karatović, David; ...; ...

Source / Izvornik: **Nature Physics, 2022, 19, 61 - 71**

Journal article, Published version

Rad u časopisu, Objavljena verzija rada (izdavačev PDF)

<https://doi.org/10.1038/s41567-022-01804-8>

Permanent link / Trajna poveznica: <https://urn.nsk.hr/urn:nbn:hr:217:643345>

Rights / Prava: [Attribution 4.0 International](#)/[Imenovanje 4.0 međunarodna](#)

Download date / Datum preuzimanja: **2025-03-29**



Repository / Repozitorij:

[Repository of the Faculty of Science - University of Zagreb](#)



Measurement of anti- ${}^3\text{He}$ nuclei absorption in matter and impact on their propagation in the Galaxy

Received: 18 February 2022

Accepted: 21 September 2022

Published online: 12 December 2022

 Check for updatesThe ALICE Collaboration* 


In our Galaxy, light antinuclei composed of antiprotons and antineutrons can be produced through high-energy cosmic-ray collisions with the interstellar medium or could also originate from the annihilation of dark-matter particles that have not yet been discovered. On Earth, the only way to produce and study antinuclei with high precision is to create them at high-energy particle accelerators. Although the properties of elementary antiparticles have been studied in detail, the knowledge of the interaction of light antinuclei with matter is limited. We determine the disappearance probability of ${}^3\overline{\text{He}}$ when it encounters matter particles and annihilates or disintegrates within the ALICE detector at the Large Hadron Collider. We extract the inelastic interaction cross section, which is then used as an input to the calculations of the transparency of our Galaxy to the propagation of ${}^3\overline{\text{He}}$ stemming from dark-matter annihilation and cosmic-ray interactions within the interstellar medium. For a specific dark-matter profile, we estimate a transparency of about 50%, whereas it varies with increasing ${}^3\overline{\text{He}}$ momentum from 25% to 90% for cosmic-ray sources. The results indicate that ${}^3\overline{\text{He}}$ nuclei can travel long distances in the Galaxy, and can be used to study cosmic-ray interactions and dark-matter annihilation.

There are no natural forms of antinuclei on Earth, but we know they exist because of fundamental symmetries in particle physics and their observation in interactions of high-energy accelerated beams. Light antinuclei, objects composed of antiprotons (\overline{p}) and antineutrons (\overline{n}), such as \overline{d} (\overline{pn}), ${}^3\overline{\text{He}}$ (\overline{ppn}) and ${}^4\overline{\text{He}}$ (\overline{ppnn}), have been produced and studied at various accelerator facilities^{1–18}, including precision measurements of the mass difference between nuclei and antinuclei^{19,20}. The interest in the properties of such objects is manifold. From the nuclear physics perspective, the production mechanism and interactions of antinuclei can elucidate the detailed features of the strong interaction that binds nucleons into nuclei²¹. From the astrophysical standpoint, natural sources of antinuclei may include the annihilation of dark-matter (DM) particles such as weakly interacting massive particles²² and other exotic sources such as antistars^{23,24}. DM constitutes about 27% of the total energy density budget within our Universe²⁵.

This is demonstrated by the measurement of the fine structure of the cosmic microwave background^{26,27}, gravitational lensing of galaxy clusters²⁸ and the rotational curves of some galaxies²³. Another possible source of antinuclei in our Universe is high-energy cosmic-ray collisions with atoms in the interstellar medium.

The observation of antinuclei such as ${}^3\overline{\text{He}}$ is one of the most promising signatures of DM annihilation of weakly interacting massive particles^{22,29–32}. The kinetic-energy distribution of antinuclei produced in DM annihilation peaks at low kinetic energies (E_{kin} per nucleon $\lesssim 1 \text{ GeV } A^{-1}$) for most assumptions of DM mass²². In contrast, for antinuclei originating from cosmic-ray interactions, the spectrum peaks at much larger E_{kin} per nucleon ($\sim 10 \text{ GeV } A^{-1}$). Thus, the low-energy region is almost free of background for DM searches.

To calculate the expected flux of antinuclei near Earth, one needs to precisely know the antinucleus formation and annihilation

*A list of authors and their affiliations appears at the end of the paper.  e-mail: alice-publications@cern.ch

probabilities in the Galaxy. The formation probability of light antinuclei (up to mass number $A = 4$) is currently studied at accelerators. By now, several models successfully describe light-antinuclei production yields^{33–37}. Such models are based on either the statistical hadronization^{12,38–40} or coalescence approach^{41–45}.

Another crucial aspect in the search of antinuclei in our Galaxy is the knowledge of their disappearance probability when they encounter matter and annihilate or disintegrate. Antinuclei generated in our Galaxy may travel thousands of light years⁴⁶ before reaching the Earth and being detected. The journey of antinuclei through the Galaxy can be modelled by propagation codes, which incorporate the initial distribution of antinucleus sources, interstellar gas distribution in the Galaxy, elastic scatterings and inelastic hadronic interactions with the interstellar medium. The antinucleus flux in the Solar System is further modulated by solar magnetic fields. During the entire journey, antinuclei can encounter matter and disappear. The disappearance probability is quantified through the inelastic cross section. It is normally studied employing particle beams of interest impinging on targets of known composition and thickness, but antinuclei beams are very challenging to obtain. Today, the Large Hadron Collider (LHC) is the best facility to study nuclear antimatter since its high energies allow one to produce, on average, as many nuclei as antinuclei in proton–proton (pp) and lead–lead (Pb–Pb) collisions^{12,47}. The detector material can serve as the target and the disappearance probability can be experimentally determined⁴⁸.

This work presents the measurement of the ${}^3\overline{\text{He}}$ inelastic cross section $\sigma_{\text{inel}}({}^3\overline{\text{He}})$, obtained using data from the ALICE experiment. These results are used in model calculations to assess the effect of the disappearance of antinuclei during their propagation through our Galaxy. The associated uncertainties are estimated based on experimental data. The transparency of our Galaxy to the propagation of ${}^3\overline{\text{He}}$ nuclei stemming from a specific DM source and from interactions of high-energy cosmic rays with the interstellar medium is determined, providing one of the necessary constraints for the study of antinuclei in space.

Determination of the inelastic cross section

The measurement of the inelastic cross sections under controlled conditions requires a beam with a well-defined momentum and a target whose material and its spatial distribution are well known. Since no ${}^3\overline{\text{He}}$ beams are available, we exploit the antimatter production at the LHC and the excellent identification and momentum determination for ${}^3\overline{\text{He}}$ in ALICE as an equivalent setup. In our study, the ALICE detector itself serves as the target for inelastic processes. A detailed description of the detector and its performance is available elsewhere^{49,50}. Here, serving as probes, ${}^3\overline{\text{He}}$ and ${}^3\text{He}$ nuclei are produced in pp and Pb–Pb collisions. At LHC high energies, ${}^3\overline{\text{He}}$ and ${}^3\text{He}$ are produced in the same amounts on average. The primordial ratio can be derived from precise antiproton-to-proton measurements^{47,51} and in pp collisions at the centre-of-mass energy of $\sqrt{s} = 13$ TeV corresponds to 0.994 ± 0.045 . The ALICE subdetectors that are considered as targets

are the inner tracking system (ITS), the time projection chamber (TPC) and the transition radiation detector (TRD). A schematic of the ALICE detector is shown in Fig. 1a. The material composition of the three subdetectors is diverse. The detailed knowledge of the detector geometry and composition^{50,52} (see the Supplemental Material of ref. 48 for a cumulative distribution of the material in the ALICE apparatus) enables the determination of the effective target material for this layered configuration (Methods). Here $\sigma_{\text{inel}}({}^3\overline{\text{He}})$ can be estimated for three effective targets. The first one is characterized by the average material of the ITS + TPC systems (with averaged atomic mass and charge numbers of $\langle A \rangle = 17.4$ and $\langle Z \rangle = 8.5$, respectively), the second one corresponds to the ITS + TPC + TRD systems ($\langle A \rangle = 31.8$ and $\langle Z \rangle = 14.8$)⁴⁸ and the third one corresponds to the TRD system only ($\langle A \rangle = 34.7$ and $\langle Z \rangle = 16.1$). The values are obtained by weighting the contribution from different materials with their density times the length crossed by particles.

Figure 1 shows a schematic of the analysis steps necessary to extract $\sigma_{\text{inel}}({}^3\overline{\text{He}})$. Figure 1a shows the ${}^3\overline{\text{He}}$ and ${}^3\text{He}$ tracks crossing the ALICE detector, with the annihilation occurring for ${}^3\overline{\text{He}}$. The momentum p is measured via the determination of the track trajectory and curvature radius in the ALICE magnetic field ($B = 0.5$ T). Here ${}^3\overline{\text{He}}$ and ${}^3\text{He}$ are first identified when they reach the TPC by the measurement of their specific energy loss (dE/dx) in the detector gas. The excellent separation power of this measurement is shown in Fig. 1b, where dE/dx is presented as a function of particle rigidity (p/z) and z denotes the charge of the particle crossing the TPC in units of electron charge. Here the red dots represent all the nuclei that are reconstructed in the TPC, whereas the blue dots show the nuclei that survive up to the time-of-flight (TOF) detector where they are matched to a TOF hit. A more detailed description of the employed particle identification methods can be found in Methods.

We use two methods to evaluate $\sigma_{\text{inel}}({}^3\overline{\text{He}})$. The first method, applied to the pp data sample at $\sqrt{s} = 13$ TeV, relies on the comparison of the measured ${}^3\overline{\text{He}}$ and ${}^3\text{He}$ yields (antibaryon-to-baryon method). In this case, the experimental observable is constituted by the reconstructed ${}^3\overline{\text{He}}/{}^3\text{He}$ ratio analogously to the method used elsewhere⁴⁸ for (anti)deuterons. The inelastic process that takes place in the ITS, TPC or TRD material manifests itself by the fact that fewer ${}^3\overline{\text{He}}$ than ${}^3\text{He}$ candidates are detected (Fig. 1c). Both destructive and non-destructive inelastic processes contribute to this effect. Here the full circular blue symbols show the momentum-dependent ${}^3\overline{\text{He}}/{}^3\text{He}$ ratio measured in pp collisions as a function of the particle rigidity reconstructed at the primary vertex ($p_{\text{primary}}/|z|$). The discontinuity of the ${}^3\overline{\text{He}}/{}^3\text{He}$ ratio observed at $p_{\text{primary}}/|z| = 1$ GeV c^{-1} is due to the additional requirement of a hit in the TOF detector for momenta above this value. This ratio can also be evaluated by means of a full-scale Monte Carlo (MC) simulation of antinuclei and nuclei traversing the ALICE detector.

The measured observables are compared in each momentum interval with simulations where $\sigma_{\text{inel}}({}^3\overline{\text{He}})$ is varied to obtain the inelastic cross sections. We performed several full-scale simulations with variations in $\sigma_{\text{inel}}({}^3\overline{\text{He}})$ with respect to the standard parameterization

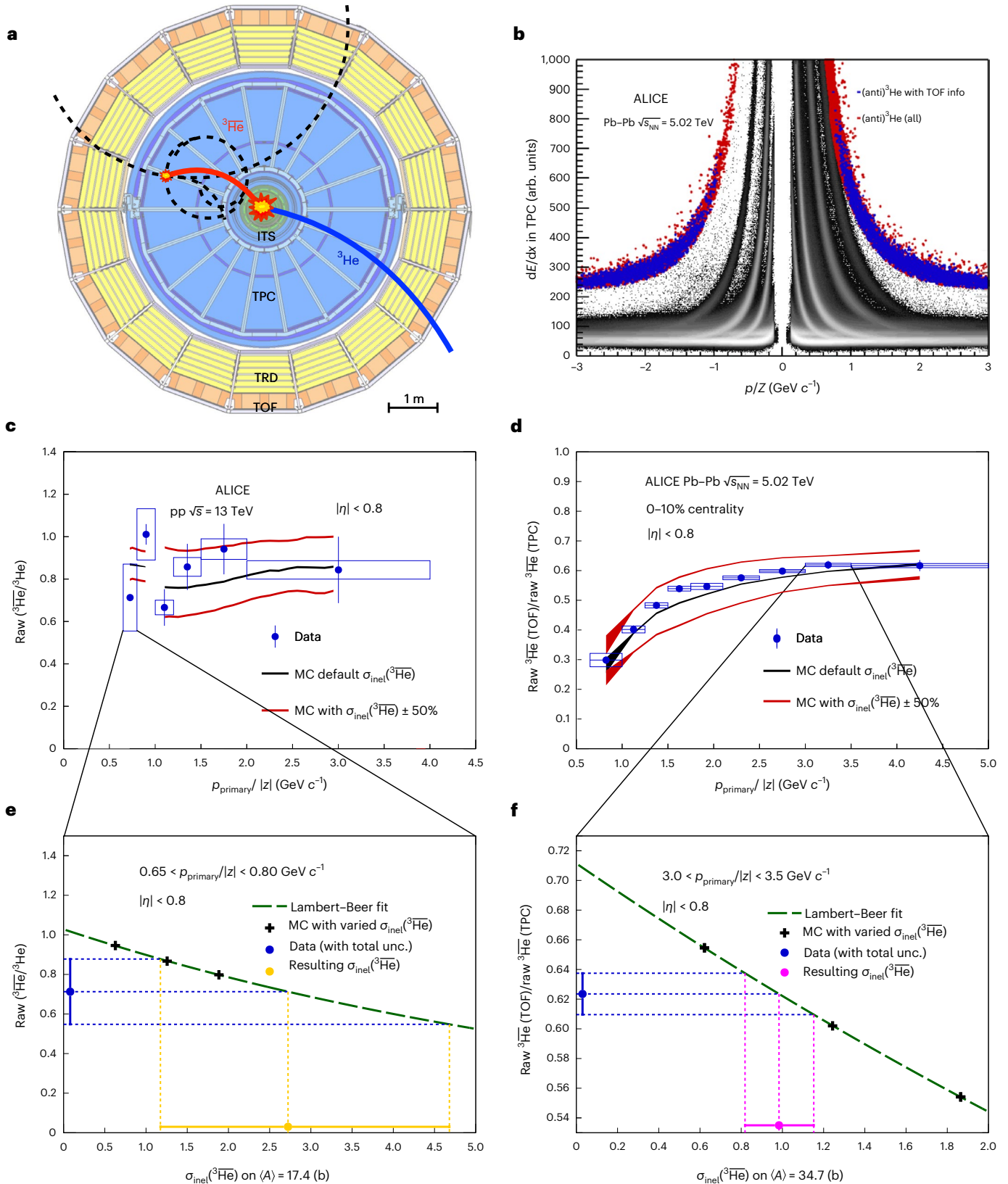
Fig. 1 | Description of the steps followed for the extraction of $\sigma_{\text{inel}}({}^3\overline{\text{He}})$. a, Schematic of the ALICE detectors at midrapidity in the plane perpendicular to the beam axis, with the collision point located in the middle; the ITS, TPC, TRD and TOF detectors are shown in green, blue, yellow and orange, respectively. A ${}^3\overline{\text{He}}$ that annihilates in the TPC gas is shown in red, and a ${}^3\text{He}$ that does not undergo an inelastic reaction and reaches the TOF detector is shown in blue; the dashed curves represent charged (anti)particles produced in the ${}^3\overline{\text{He}}$ annihilation. **b**, Identification of (anti)nuclei by means of their specific energy loss dE/dx and momentum measurement in the TPC. The red points show all the (anti) ${}^3\text{He}$ nuclei reconstructed with the TPC detector, and the blue points correspond to (anti) ${}^3\text{He}$ with TOF information; other (anti)particles are shown in black. **c**, Experimental results for the raw ratio of ${}^3\overline{\text{He}}$ to ${}^3\text{He}$ in pp collisions at $\sqrt{s} = 13$ TeV as a function of rigidity. The vertical lines and boxes represent

statistical and systematic uncertainties in terms of standard deviations, respectively. The black and red lines show the results from the MC simulations with varied $\sigma_{\text{inel}}({}^3\overline{\text{He}})$. **d**, Experimental ratio of ${}^3\overline{\text{He}}$ with TOF information over ${}^3\overline{\text{He}}$ reconstructed in the TPC in the 10% most central Pb–Pb collisions at $\sqrt{s_{\text{NN}}} = 5.02$ TeV as a function of rigidity. The black and red lines show the results from the MC simulations with varied $\sigma_{\text{inel}}({}^3\overline{\text{He}})$ values. **e**, Raw ratio of ${}^3\overline{\text{He}}$ to ${}^3\text{He}$ in a particular rigidity interval as a function of $\sigma_{\text{inel}}({}^3\overline{\text{He}})$ for $\langle A \rangle = 17.4$. The fit to the results from MC simulations (black points) shows the dependence of the observable on $\sigma_{\text{inel}}({}^3\overline{\text{He}})$ according to the Lambert–Beer formula. The horizontal dashed blue lines show the central value and 1σ uncertainties for the measured observable and their intersection with the Lambert–Beer function determines $\sigma_{\text{inel}}({}^3\overline{\text{He}})$ limits (yellow lines). **f**, Extraction of $\sigma_{\text{inel}}({}^3\overline{\text{He}})$ for $\langle A \rangle = 34.7$ analogous to the data in **e**, with $\sigma_{\text{inel}}({}^3\overline{\text{He}})$ limits shown as the magenta lines.

implemented in the Geant4 package^{53,54} (Fig. 1c). Figure 1e presents the simulated ratio as a function of $\sigma_{\text{inel}}(^3\text{He})$ parameterized using the Lambert–Beer law⁵⁵. For each momentum interval, the uncertainties of $\sigma_{\text{inel}}(^3\text{He})$ are obtained by requiring an agreement at $\pm 1\sigma$ with the measured observables, where σ represents the total experimental

uncertainty (statistical and systematic uncertainties added in quadrature).

The second method, employed in the Pb–Pb data analysis at a centre-of-mass energy per nucleon pair $\sqrt{s_{\text{NN}}} = 5.02$ TeV, measures the disappearance of ^3He nuclei in the TRD detector only (TOF-to-TPC



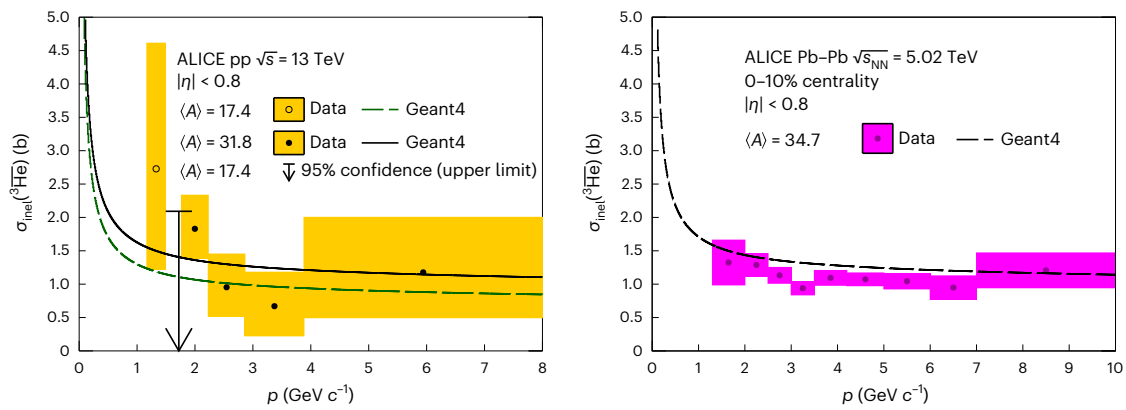


Fig. 2 | Results for $\sigma_{\text{inel}}(^3\text{He})$ as a function of ^3He momentum. Results obtained from pp collisions at $\sqrt{s} = 13$ TeV (left); results from the 10% most central Pb–Pb collisions at $\sqrt{s_{\text{NN}}} = 5.02$ TeV (right). The curves represent the Geant4 cross sections corresponding to the effective material probed by the different

analyses. The arrow on the left plot shows the 95% confidence limit on $\sigma_{\text{inel}}(^3\text{He})$ for $\langle A \rangle = 17.4$. The different values of $\langle A \rangle$ correspond to the three different effective targets (see the main text for details). All the indicated uncertainties represent standard deviations.

method). The ratio of ^3He with TOF information to all the ^3He candidates is considered as an experimental observable. Figure 1d shows the momentum-dependent ratio of ^3He with a reconstructed TOF hit to all the ^3He candidates extracted from Pb–Pb collisions. As with the first method, this observable is also evaluated by means of a full-scale MC Geant4 simulation assuming different $\sigma_{\text{inel}}(^3\text{He})$ values. Figure 1f shows the extraction of $\sigma_{\text{inel}}(^3\text{He})$ and its related uncertainties for one rigidity interval following the same procedure as the one used in the first method.

The final results are shown in Fig. 2. Figure 2 (left) shows the $\sigma_{\text{inel}}(^3\text{He})$ results from the pp data analysis with the yellow boxes representing the $\pm 1\sigma$ uncertainty intervals. In Fig. 2 (right), the histogram with the magenta error boxes shows $\sigma_{\text{inel}}(^3\text{He})$ extracted from the Pb–Pb data analysis. The results are shown as a function of momentum p at which the inelastic interaction occurs. Due to continuous energy loss inside the detector material, this momentum is lower than p_{primary} reconstructed at the primary vertex (Methods). The antibaryon-to-baryon ratio method is applied in the pp data analysis, enabling the measurement of $\sigma_{\text{inel}}(^3\text{He})$ down to a low momentum. The copious background makes this method inapplicable in Pb–Pb collisions below $p = 1.5$ GeV c^{-1} (Methods). The TOF-to-TPC method is unavailable in this momentum range since ^3He nuclei do not reach the TOF due to the large energy loss and bending within the magnetic field. On the other hand, for momentum values larger than $p = 1.5$ GeV c^{-1} , the yield of produced ^3He is substantially larger in Pb–Pb collisions, thus leading to higher statistical precision for this colliding system using the TOF-to-TPC method. The evaluation of systematic uncertainties is described in Methods. These two independent analysis methods, therefore, provide access to slightly different momentum ranges and to different $\langle A \rangle$ values and deliver consistent results in the common momentum region.

The cross section used by Geant4 for the average mass number $\langle A \rangle$ of the material is shown by the dashed lines in Fig. 2. It is obtained from a Glauber model parameterization⁵⁴ of the collisions of ^3He with the target nuclei in which the antinucleon–nucleon cross-section value is taken from the measured $\bar{p}p$ collisions⁵⁶. Agreement with the experimental $\sigma_{\text{inel}}(^3\text{He})$ value is observed within two standard deviations in the studied momentum range.

Propagation of antinuclei in the interstellar medium

To estimate the transparency of our Galaxy to ^3He nuclei, we consider two examples of ^3He production sources. Results from another work⁵⁷ are used as the input for the production cross section of ^3He from

cosmic-ray collisions with the interstellar medium. As a DM source of ^3He , we consider weakly interacting massive particle candidates with a mass of 100 GeV c^{-2} annihilating into W^+W^- pairs followed by hadronization into (anti)nuclei²⁹. In both cases, the yields of produced ^3He are determined by employing the coalescence model that builds antinuclei from antineutrons and antiprotons that are close-by in the phase space^{12,41,42}. More details about the cosmic-ray and DM sources are discussed in Methods. Additional ^3He sources such as supernovae remnants⁵⁸, antistars^{23,24} and primordial black holes^{59–61} have not been included in this work.

We consider the DM density distribution in our Galaxy according to the Navarro–Frenk–White profile⁶² (Fig. 3, top), where a schematic of the ^3He production from cosmic-ray interaction with the interstellar gas or DM annihilations is also shown.

The propagation of charged particles within galaxies is driven by magnetic fields. The propagation is commonly described by a transport equation that includes the following terms: (1) a source function; (2) diffusion; (3) convection; (4) momentum variations due to Coulomb scattering, diffusion and ionization processes; (5) fragmentation, decays and inelastic interactions. This equation, discussed in more detail in Methods, can be numerically solved by employing several propagation models^{63–66}. In this work, the publicly available GALPROP code⁶⁶ is employed. In the context of this calculation, our Galaxy is approximated by a cylindrical disk filled with an interstellar gas composed of hydrogen (~90%) and ^4He (~10%) with an average hydrogen number density of ~ 1 atom cm^{-3} (ref. 67). The gas distribution within our Galaxy is constrained by several astronomical spectroscopy measurements^{68–71}. GALPROP provides the propagation of particles up to the boundaries of the Solar System. To estimate the particle flux inside the Solar System, the effect of the solar magnetic field must be taken into account. This can be achieved by employing the force-field approximation or dedicated models like HelMod^{72,73}. The whole propagation chain is benchmarked using several species of cosmic rays, including protons and light nuclei (up to $Z = 28$)⁴⁶. The cosmic-ray injection spectra and the propagation parameters are tuned to match the measurements of protons and light nuclei both outside⁷⁴ and within^{75–77} the Solar System.

After their production, the ^3He nuclei need to travel a distance of several kiloparsecs to reach Earth^{46,62}. During this passage, they might encounter protons or ^4He nuclei in interstellar gas and inelastically interact. Non-destructive inelastic processes can occur and cause a substantial energy loss that results in a so-called tertiary ^3He source peaked at low kinetic energies. Such a tertiary source component, however, only contributes a few percent of the total flux^{30,31}. We neglect

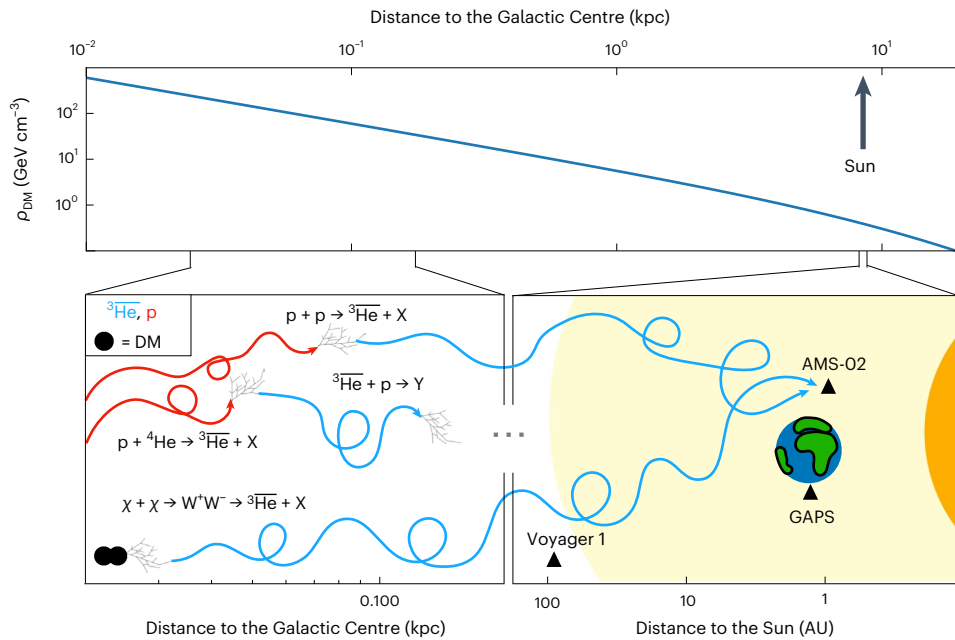


Fig. 3 | Schematic of ${}^3\text{He}$ production and propagation in our Galaxy. Distribution of DM density ρ_{DM} in our Galaxy as a function of distance from the Galactic Centre according to the Navarro–Frenk–White profile⁶² (top). Graphical illustration of ${}^3\text{He}$ production from cosmic-ray interactions with interstellar gas

or DM (χ) annihilations (bottom). The yellow halo represents the heliosphere and the Earth, Sun and positions of the Voyager 1, AMS-02 and GAPS experiments are depicted, too.

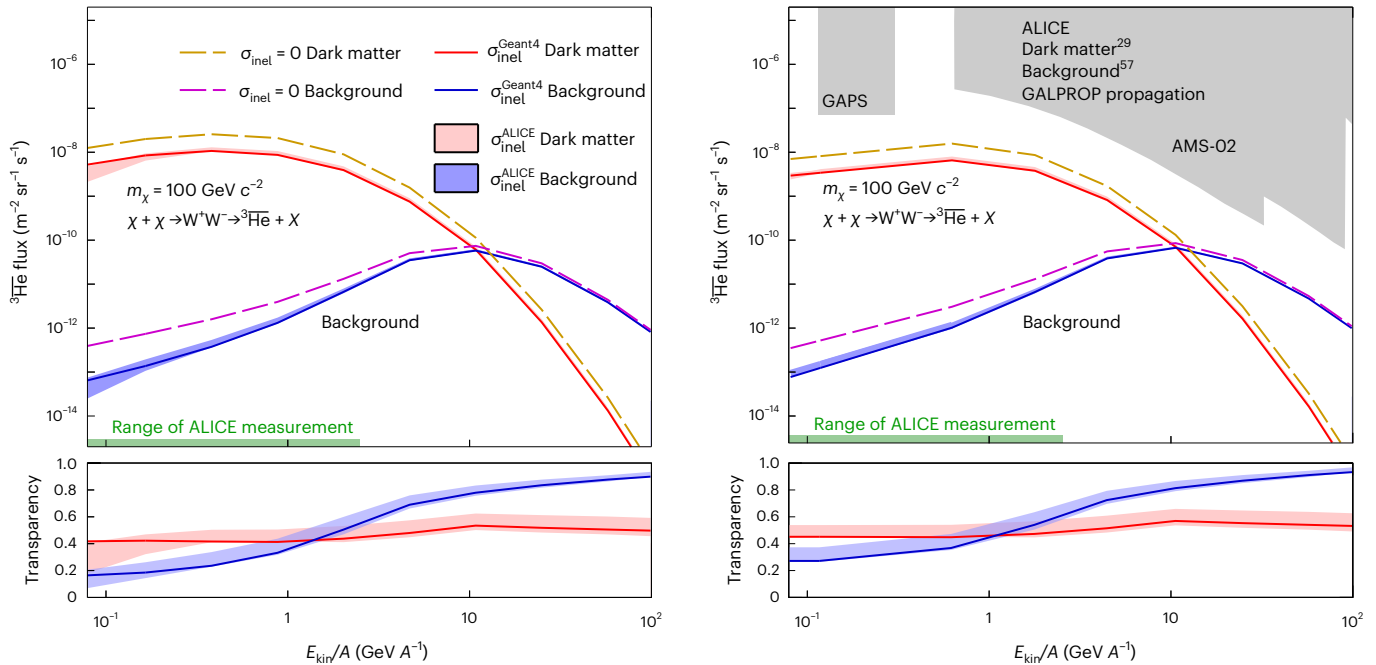


Fig. 4 | Expected ${}^3\text{He}$ flux near Earth before and after solar modulation. Data before (left) and after (right) solar modulation. The latter is obtained using the force-field method with modulation potential $\phi = 400$ MV. The results are shown as a function of kinetic energy per nucleon (E_{kin}/A). Fluxes for DM signal χ (red) and cosmic-ray background (blue) antihelium nuclei for different cases of inelastic cross sections used in the calculations (top). The bands show the results obtained with $\sigma_{\text{inel}}({}^3\text{He})$ from ALICE measurements, and the full lines correspond to the results using the parameterizations. The dashed lines show the fluxes obtained with $\sigma_{\text{inel}}({}^3\text{He})$ set to zero for the DM signal (orange line) and for the

cosmic-ray background (magenta line). The green band on the x axis indicates the kinetic-energy range corresponding to the ALICE measurement for $\sigma_{\text{inel}}({}^3\text{He})$. Transparency of our Galaxy to the propagation of ${}^3\text{He}$ outside (left) and inside (right) the Solar System (bottom). The shaded areas (top right) show the expected sensitivity of the GAPS⁷⁹ and AMS-02³⁰ experiments. The top panels also show the fluxes obtained with $\sigma_{\text{inel}}({}^3\text{He})$ set to zero. Only the uncertainties relative to the measured $\sigma_{\text{inel}}({}^3\text{He})$ are shown, which represent standard deviations. The calculations employ the ${}^3\text{He}$ DM source described elsewhere²⁹ and the ${}^3\text{He}$ production cross section from the cosmic-ray background⁵⁷.

this small contribution because we cannot distinguish between destructive and non-destructive inelastic processes. To model the total cross section of inelastic processes, we scale the momentum-dependent Geant4 parameterization of the ${}^3\text{He}-p$ inelastic cross section with the correction factors obtained from our measurements. For the low-momentum range ($1.17 \leq p < 1.50 \text{ GeV } c^{-1}$), we consider the results from pp collisions and for the high-momentum range ($1.50 \leq p < 10.00 \text{ GeV } c^{-1}$), results from Pb–Pb collisions. The correction factors from the ALICE measurements and their uncertainties are parameterized with a continuous function employing a combination of polynomial and exponential functions. The additional uncertainty due to scaling with A is estimated to be lower than 8% (ref. ⁵⁴) (Methods). For the extrapolation to momenta above the measured momentum range, we consider the correction factor corresponding to the last measured momentum interval (Fig. 2, right). The resulting ${}^3\text{He}-p$ inelastic cross section as a function of the ${}^3\text{He}$ kinetic energy per nucleon is shown in Extended Data Fig. 1 together with the Geant4 parameterization and the model employed in another work³⁰. The same procedure is applied to describe the ${}^3\text{He}-{}^4\text{He}$ inelastic processes. These scaled inelastic cross sections have been implemented in GALPROP.

The expected ${}^3\text{He}$ flux near Earth after all the propagation steps (Methods) with and without the effect of solar modulations is shown in the right and left panels of Fig. 4, respectively. Solar modulation is implemented using the force-field method⁷². The effect of inelastic interactions is demonstrated by showing the full propagation chain once with $\sigma_{\text{inel}}({}^3\text{He})$ set to zero and once with the inelastic cross section extracted from the ALICE measurement. Only the uncertainties relative to the measured $\sigma_{\text{inel}}({}^3\text{He})$ value are propagated and presented in Fig. 4. The inelastic collisions of ${}^3\text{He}$ with interstellar gas lead to a notable reduction in the expected flux for the signal candidates from DM as well as the background from cosmic-ray collisions.

The transparency of our Galaxy to the ${}^3\text{He}$ passage is defined by the ratio of the flux obtained with and without the inelastic processes in GALPROP. The transparency values as a function of kinetic energy obtained with $\sigma_{\text{inel}}({}^3\text{He})$ from the Geant4 parameterization and from the ALICE measurements are shown in Fig. 4 (bottom) by the coloured lines and bands, respectively. The transparency profiles obtained with a solar modulation potential of 400 MV do not differ much from the non-modulated distributions (Fig. 4, bottom left and right). This is because the solar modulation reshuffles the yield from the more abundant high-momentum range to lower energies, but all the transparency profiles are rather flat as a function of particle energy. A transparency of the Galaxy of about 50% is estimated for ${}^3\text{He}$ from the considered DM source²⁹ and of about 25% for low-energy ${}^3\text{He}$ from cosmic-ray interactions⁵⁷. The latter increases further up to full transparency at higher energies. The different behaviour in the two cases is caused by both different underlying spectral shapes and different distributions of production points of the two sources, underlining the importance of full propagation studies (Methods). The employment of an alternative set of propagation parameters from ref. ⁷⁸ results in 40–60% lower transparency at low E_{kin} than using the propagation parameters from ref. ⁴⁶ (Methods).

The calculated ${}^3\text{He}$ transparency is found to be consistent—within uncertainties—with the Geant4 parameterization. It must be clearly noted that previously, it was not possible to quantify the uncertainty of the parameterizations employed in Geant4 or proposed elsewhere³⁰ due to the lack of experimental data. To quantify the improvement originating from our study, we, therefore, simply compare the full difference between no inelastic interaction and alternative parameterizations (~50% for the signal from DM and up to 75% for background) to our newly established uncertainties of about 10%–15% after solar modulation. We have, thus, verified that the uncertainty related to nuclear absorption is subleading with respect to other possible contributions in the cosmic-ray and DM modelling, particularly the production mechanism and propagation description^{29–31,57}. Note that the

propagation example provided in this work does not cover the full range of uncertainties related to ${}^3\text{He}$ flux modelling (Methods); rather, it delivers a clear road map for future studies. The measured $\sigma_{\text{inel}}({}^3\text{He})$ and the developed methodology can be employed to carry out the propagation of ${}^3\text{He}$ using any DM or cosmic-ray interaction modelling as a source. Since a large separation between the signal and background is retained for low kinetic energies, our results clearly underline that the search for ${}^3\text{He}$ in space remains a very promising channel for the discovery of DM. These studies will be extended to ${}^4\text{He}$ and to the lower-momentum region in the near future with much larger datasets that will be collected in the coming few years.

Online content

Any methods, additional references, Nature Portfolio reporting summaries, source data, extended data, supplementary information, acknowledgements, peer review information; details of author contributions and competing interests; and statements of data and code availability are available at <https://doi.org/10.1038/s41567-022-01804-8>.

References

1. NA44 Collaboration Deuteron and anti-deuteron production in CERN experiment NA44. *Nucl. Phys. A* **590**, 483C–486C (1995).
2. E864 Collaboration et al. Anti-deuteron yield at the AGS and coalescence implications. *Phys. Rev. Lett.* **85**, 2685–2688 (2000).
3. NA49 Collaboration et al. Deuteron production in central Pb+Pb collisions at 158A GeV. *Phys. Lett. B* **486**, 22–28 (2000).
4. NA49 Collaboration et al. Energy and centrality dependence of deuteron and proton production in Pb+Pb collisions at relativistic energies. *Phys. Rev. C* **69**, 024902 (2004).
5. PHENIX Collaboration et al. Deuteron and antideuteron production in Au+Au collisions at $\sqrt{s_{\text{NN}}}=200 \text{ GeV}$. *Phys. Rev. Lett.* **94**, 122302 (2005).
6. Alper, B. et al. Large angle production of stable particles heavier than the proton and a search for quarks at the CERN intersecting storage rings. *Phys. Lett. B* **46**, 265–268 (1973).
7. British-Scandinavian-MIT Collaboration et al. Production of deuterons and anti-deuterons in proton proton collisions at the CERN ISR. *Lett. Nuovo Cim.* **21**, 189–194 (1978).
8. Alexopoulos, T. et al. Cross-sections for deuterium, tritium, and helium production in $\bar{p}p$ collisions at $\sqrt{s}=1.8 \text{ TeV}$. *Phys. Rev. D* **62**, 072004 (2000).
9. H1 Collaboration Measurement of anti-deuteron photoproduction and a search for heavy stable charged particles at HERA. *Eur. Phys. J. C* **36**, 413–423 (2004).
10. CLEO Collaboration et al. Anti-deuteron production in $\Upsilon(nS)$ decays and the nearby continuum. *Phys. Rev. D* **75**, 012009 (2007).
11. ALEPH Collaboration et al. Deuteron and anti-deuteron production in e^+e^- collisions at the Z resonance. *Phys. Lett. B* **639**, 192–201 (2006).
12. ALICE Collaboration et al. Production of light nuclei and anti-nuclei in pp and Pb-Pb collisions at energies available at the CERN Large Hadron Collider. *Phys. Rev. C* **93**, 024917 (2016).
13. ALICE Collaboration et al. ${}^3\text{H}$ and ${}^3\bar{\text{H}}$ production in Pb–Pb collisions at $\sqrt{s_{\text{NN}}}=2.76 \text{ TeV}$. *Phys. Lett.* **B754**, 360–372 (2016).
14. ALICE Collaboration et al. Measurement of deuteron spectra and elliptic flow in Pb–Pb collisions at $\sqrt{s_{\text{NN}}}=2.76 \text{ TeV}$ at the LHC. *Eur. Phys. J.* **C77**, 658 (2017).
15. ALICE Collaboration et al. Multiplicity dependence of (anti-)deuteron production in pp collisions at $\sqrt{s}=7 \text{ TeV}$. *Phys. Lett.* **B794**, 50–63 (2019).
16. STAR Collaboration et al. Observation of the antimatter helium-4 nucleus. *Nature* **473**, 353–356 (2011).
17. STAR Collaboration et al. Observation of an antimatter hypernucleus. *Science* **328**, 58–62 (2010).

18. STAR Collaboration et al. \bar{d} and ${}^3\text{He}$ production in $\sqrt{s_{\text{NN}}}=130\text{ GeV}$ Au+Au collisions. *Phys. Rev. Lett.* **87**, 262301 (2001); erratum **87**, 279902 (2001).
19. ALICE Collaboration et al. Precision measurement of the mass difference between light nuclei and anti-nuclei. *Nat. Phys.* **11**, 811–814 (2015).
20. STAR Collaboration et al. Measurement of the mass difference and the binding energy of the hypertriton and antihypertriton. *Nat. Phys.* **16**, 409–412 (2020).
21. STAR Collaboration et al. Measurement of interaction between antiprotons. *Nature* **527**, 345–348 (2015).
22. Ibarra, A. & Wild, S. Prospects of antideuteron detection from dark matter annihilations or decays at AMS-02 and GAPS. *JCAP* **02**, 021 (2013).
23. Persic, M., Salucci, P. & Stel, F. The universal rotation curve of spiral galaxies—1. The dark matter connection. *Mon. Not. R. Astron. Soc.* **281**, 27–47 (1996).
24. Poulin, V. et al. Where do the AMS-02 antihelium events come from? *Phys. Rev. D* **99**, 023016 (2019).
25. Planck Collaboration et al. Planck 2018 results. VI. Cosmological parameters. *Astron. Astrophys.* **641**, A6 (2020).
26. Bond, J. & Efstathiou, G. Cosmic background radiation anisotropies in universes dominated by nonbaryonic dark matter. *Astrophys. J. Lett.* **285**, L45–L48 (1984).
27. Boomerang Collaboration et al. A flat universe from high resolution maps of the cosmic microwave background radiation. *Nature* **404**, 955–959 (2000).
28. Clowe, D. et al. A direct empirical proof of the existence of dark matter. *Astrophys. J. Lett.* **648**, L109–L113 (2006).
29. Carlson, E. et al. Antihelium from dark matter. *Phys. Rev. D* **89**, 076005 (2014).
30. Korsmeier, M., Donato, F. & Fornengo, N. Prospects to verify a possible dark matter hint in cosmic antiprotons with antideuterons and antihelium. *Phys. Rev.* **D97**, 103011 (2018).
31. von Doetinchem, P. et al. Cosmic-ray antinuclei as messengers of new physics: status and outlook for the new decade. *JCAP* **08**, 035 (2020).
32. Winkler, M. W. & Linden, T. Dark matter annihilation can produce a detectable antihelium flux through $\bar{\Lambda}_b$ decays. *Phys. Rev. Lett.* **126**, 101101 (2021).
33. Bellini, F., Blum, K., Kalweit, A. P. & Puccio, M. Examination of coalescence as the origin of nuclei in hadronic collisions. *Phys. Rev. C* **103**, 014907 (2021).
34. Kachelriess, M., Ostapchenko, S. & Tjemsland, J. On nuclear coalescence in small interacting systems. *Eur. Phys. J. A* **57**, 167 (2021).
35. Braun-Munzinger, P. & Dönigus, B. Loosely-bound objects produced in nuclear collisions at the LHC. *Nucl. Phys. A* **987**, 144–201 (2019).
36. Steinheimer, J. et al. Hypernuclei, dibaryon and antinuclei production in high energy heavy ion collisions: thermal production versus coalescence. *Phys. Lett. B* **714**, 85–91 (2012).
37. Braun-Munzinger, P. & Stachel, J. Production of strange clusters and strange matter in nucleus-nucleus collisions at the AGS. *J. Phys. G* **21**, L17–L20 (1995).
38. Andronic, A., Braun-Munzinger, P., Stachel, J. & Stoecker, H. Production of light nuclei, hypernuclei and their antiparticles in relativistic nuclear collisions. *Phys. Lett.* **B697**, 203–207 (2011).
39. Cleymans, J. et al. Antimatter production in proton-proton and heavy-ion collisions at ultrarelativistic energies. *Phys. Rev. C* **84**, 054916 (2011).
40. Vovchenko, V., Dönigus, B. & Stoecker, H. Multiplicity dependence of light nuclei production at LHC energies in the canonical statistical model. *Phys. Lett.* **B785**, 171–174 (2018).
41. Butler, S. & Pearson, C. Deuterons from high-energy proton bombardment of matter. *Phys. Rev.* **129**, 836–842 (1963).
42. Scheibl, R. & Heinz, U. W. Coalescence and flow in ultrarelativistic heavy ion collisions. *Phys. Rev.* **C59**, 1585–1602 (1999).
43. Blum, K. & Takimoto, M. Nuclear coalescence from correlation functions. *Phys. Rev. C* **99**, 044913 (2019).
44. Mrowczynski, S. Production of light nuclei in the thermal and coalescence models. *Acta Phys. Polon. B* **48**, 707–716 (2017).
45. Mrowczynski, S. Sum rule of the correlation function. *Phys. Lett. B* **345**, 393–396 (1995).
46. Boschini, M. et al. Inference of the local interstellar spectra of cosmic-ray nuclei $Z \leq 28$ with the GalProp–HelMod framework. *Astrophys. J. Suppl.* **250**, 27 (2020).
47. ALICE Collaboration, et al. Mid-rapidity anti-baryon to baryon ratios in pp collisions at $\sqrt{s}=0.9, 2.76$ and 7 TeV measured by ALICE. *Eur. Phys. J. C* **73**, 2496 (2013).
48. ALICE Collaboration et al. Measurement of the low-energy anti-deuteron inelastic cross section. *Phys. Rev. Lett.* **125**, 162001 (2020).
49. ALICE Collaboration et al. The ALICE experiment at the CERN LHC. *JINST* **3**, S08002 (2008).
50. ALICE Collaboration et al. Performance of the ALICE experiment at the CERN LHC. *Int. J. Mod. Phys.* **A29**, 1430044 (2014).
51. ALICE Collaboration et al. Midrapidity antiproton-to-proton ratio in pp collisions at $\sqrt{s}=0.9$ and 7 TeV measured by the ALICE experiment. *Phys. Rev. Lett.* **105**, 072002 (2010).
52. ALICE Collaboration. Validation of the ALICE material budget between TPC and TOF detectors. ALICE-PUBLIC-2022-001 (CERN, 2022).
53. Geant4 Collaboration et al. Geant4—a simulation toolkit. *Nucl. Instrum. Meth. Phys. Res. A* **A506**, 250–303 (2003).
54. Uzhinsky, V. et al. Antinucleus–nucleus cross sections implemented in Geant4. *Phys. Lett.* **B705**, 235–239 (2011).
55. Lambert, J. H. Photometria, sive de mensura et gradibus luminis. *Colorum et umbrae* (1760).
56. Cudell, J. et al. Hadronic scattering amplitudes: medium-energy constraints on asymptotic behavior. *Phys. Rev. D* **65**, 074024 (2002).
57. Shukla, A. et al. Large-scale simulations of antihelium production in cosmic-ray interactions. *Phys. Rev. D* **102**, 063004 (2020).
58. Tomassetti, N. & Oliva, A. Production and acceleration of antinuclei in supernova shockwaves. *Astrophys. J. Lett.* **844**, L26 (2017).
59. Herms, J., Ibarra, A., Vittino, A. & Wild, S. Antideuterons in cosmic rays: sources and discovery potential. *JCAP* **02**, 018 (2017).
60. Barrau, A. et al. Antideuterons as a probe of primordial black holes. *Astron. Astrophys.* **398**, 403–410 (2003).
61. Šerkšnytė, L. et al. Reevaluation of the cosmic antideuteron flux from cosmic-ray interactions and from exotic sources. *Phys. Rev. D* **105**, 083021 (2022).
62. Navarro, J. F., Frenk, C. S. & White, S. D. The structure of cold dark matter halos. *Astrophys. J.* **462**, 563–575 (1996).
63. Kissmann, R. Galactic cosmic ray propagation models using Picard. *J. Phys. Conf. Ser.* **837**, 012003 (2017).
64. Kissmann, R. PICARD: a novel code for the galactic cosmic ray propagation problem. *Astropart. Phys.* **55**, 37–50 (2014).
65. Evoli, C., Gaggero, D., Grasso, D. & Maccione, L. Cosmic ray nuclei, antiprotons and gamma rays in the Galaxy: a new diffusion model. *JCAP* **2008**, 018 (2008).
66. Strong, A. & Moskalenko, I. Propagation of cosmic-ray nucleons in the Galaxy. *Astrophys. J.* **509**, 212–228 (1998).
67. Moskalenko, I. V., Strong, A. W., Ormes, J. F. & Potgieter, M. S. Secondary anti-protons and propagation of cosmic rays in the Galaxy and heliosphere. *Astrophys. J.* **565**, 280–296 (2002).
68. Bronfman, L. et al. A CO survey of the southern Milky Way: the mean radial distribution of molecular clouds within the solar circle. *Astrophys. J.* **324**, 248–266 (1988).

69. Gordon, M. A. & Burton, W. B. Carbon monoxide in the Galaxy. I. The radial distribution of CO, H₂, and nucleons. *Astrophys. J.* **208**, 346–353 (1976).
70. Cordes, J. M. et al. The Galactic distribution of free electrons. *Nature* **354**, 121–124 (1991).
71. Dickey, J. M. & Lockman, F. J. H I in the Galaxy. *Annu. Rev. Astron. Astrophys.* **28**, 215–261 (1990).
72. Gleeson, L. & Axford, W. Solar modulation of Galactic cosmic rays. *Astrophys. J.* **154**, 1011–1026 (1968).
73. Boschini, M. J. et al. The HelMod model in the works for inner and outer heliosphere: from AMS to Voyager probes observations. *Adv. Space Res.* **64**, 2459–2476 (2019).
74. Cummings, A. et al. Galactic cosmic rays in the local interstellar medium: Voyager 1 observations and model results. *Astrophys. J.* **831**, 18 (2016).
75. AMS Collaboration et al. Precision measurement of the proton flux in primary cosmic rays from rigidity 1 GV to 1.8 TV with the alpha magnetic spectrometer on the International Space Station. *Phys. Rev. Lett.* **114**, 171103 (2015).
76. Engelmann, J. et al. Charge composition and energy spectra of cosmic-ray for elements from Be to Ni. Results from HEAO-3-C2. *Astron. Astrophys.* **233**, 96–111 (1990).
77. Ahn, H. et al. Measurements of cosmic-ray secondary nuclei at high energies with the first flight of the CREAM balloon-borne experiment. *Astropart. Phys.* **30**, 133–141 (2008).
78. Cuoco, A., Krämer, M. & Korsmeier, M. Novel dark matter constraints from antiprotons in light of AMS-02. *Phys. Rev. Lett.* **118**, 191102 (2017).
79. GAPS Collaboration et al. Cosmic antihelium-3 nuclei sensitivity of the GAPS experiment. *Astropart. Phys.* **130**, 102580 (2021).

Publisher's note Springer Nature remains neutral with regard to jurisdictional claims in published maps and institutional affiliations.

Open Access This article is licensed under a Creative Commons Attribution 4.0 International License, which permits use, sharing, adaptation, distribution and reproduction in any medium or format, as long as you give appropriate credit to the original author(s) and the source, provide a link to the Creative Commons license, and indicate if changes were made. The images or other third party material in this article are included in the article's Creative Commons license, unless indicated otherwise in a credit line to the material. If material is not included in the article's Creative Commons license and your intended use is not permitted by statutory regulation or exceeds the permitted use, you will need to obtain permission directly from the copyright holder. To view a copy of this license, visit <http://creativecommons.org/licenses/by/4.0/>.

© CERN 2022

The ALICE Collaboration

S. Acharya¹, D. Adamová², A. Adler³, J. Adolfsson⁴, G. Aglieri Rinella⁵, M. Agnello⁶, N. Agrawal¹⁷, Z. Ahammed¹, S. Ahmad⁸, S. U. Ahn⁹, I. Ahuja¹⁰, Z. Akbar¹¹, A. Akhmedov¹², M. Al-Turany¹³, S. N. Alam⁸, D. Aleksandrov¹⁴, B. Alessandro¹⁵, H. M. Alfanda¹⁶, R. Alfaro Molina¹⁷, B. Ali⁸, Y. Ali¹⁸, A. Alici¹⁹, N. Alizadehvandchali²⁰, A. Alkin⁵, J. Alme²¹, G. Alocco²², T. Alt²³, I. Altsybeev²⁴, M. N. Anam¹⁶, C. Andrei²⁵, D. Andreou²⁶, A. Andronic²⁷, V. Anguelov²⁸, F. Antinori²⁹, P. Antonioli⁷, C. Anuj⁸, N. Apadula³⁰, L. Aphecetche³¹, H. Appelshäuser²³, S. Arcelli¹⁹, R. Arnaldi¹⁵, I. C. Arsene³², M. Arslandok³³, A. Augustinus⁵, R. Averbeck¹³, S. Aziz³⁴, M. D. Azmi⁸, A. Badalá³⁵, Y. W. Baek³⁶, X. Bai^{13,37}, R. Bailhache²³, Y. Bailung³⁸, R. Bala³⁹, A. Balbino⁶, A. Baldisseri⁴⁰, B. Balis⁴¹, D. Banerjee⁴², Z. Banoo³⁹, R. Barbera⁴³, L. Barioglio⁴⁴, M. Barlou⁴⁵, G. G. Barnaföldi⁴⁶, L. S. Barnby⁴⁷, V. Barret⁴⁸, C. Bartels⁴⁹, K. Barth⁵, E. Bartsch²³, F. Baruffaldi⁵⁰, N. Bastid⁴⁸, S. Basu⁴, G. Batigne³¹, D. Battistini⁴⁴, B. Batyunya⁵¹, D. Bauri⁵², J. L. Bazo Alba⁵³, I. G. Bearden⁵⁴, C. Beattie³³, P. Becht¹³, I. Belikov⁵⁵, A. D. C. Bell Hechavarria²⁷, F. Bellini¹⁹, R. Bellwied²⁰, S. Belokurova²⁴, V. Belyaev⁵⁶, G. Bencedi^{46,57}, S. Beole⁵⁸, A. Bercuci²⁵, Y. Berdnikov⁵⁹, A. Berdnikova²⁸, L. Bergmann²⁸, M. G. Besoiu⁶⁰, L. Betev⁵, P. P. Bhaduri¹, A. Bhasin³⁹, I. R. Bhat³⁹, M. A. Bhat⁴², B. Bhattacharjee⁶¹, P. Bhattacharya⁶², L. Bianchi⁵⁸, N. Bianchi⁶³, J. Bielčik⁶⁴, J. Bielčikova², J. Biernat⁶⁵, A. Bilandzic⁴⁴, G. Biro⁴⁶, S. Biswas⁴², J. T. Blair⁶⁶, D. Blau^{14,67}, M. B. Blidaru¹³, C. Blume²³, G. Boca^{68,69}, F. Bock⁷⁰, A. Bogdanov⁵⁶, S. Boi⁶², J. Bok⁷¹, L. Boldizsár⁴⁶, A. Bolozdynya⁵⁶, M. Bombara¹⁰, P. M. Bond⁵, G. Bonomi^{69,72}, H. Borel⁴⁰, A. Borissov⁶⁷, H. Bossi³³, E. Botta⁵⁸, L. Bratrud²³, P. Braun-Munzinger¹³, M. Bregant⁷³, M. Broz⁶⁴, G. E. Bruno^{74,75}, M. D. Buckland^{49,76}, D. Budnikov⁷⁷, H. Buesching²³, S. Bufalino⁶, O. Bugnon³¹, P. Buhler⁷⁸, Z. Buthelezi^{79,80}, J. B. Butt¹⁸, A. Bylinkin⁸¹, S. A. Bysiak⁶⁵, M. Cai^{16,50}, H. Caines³³, A. Caliva¹³, E. Calvo Villar⁵³, J. M. M. Camacho⁸², R. S. Camacho⁸³, P. Camerini⁷⁶, F. D. M. Canedo⁷³, M. Carabas⁸⁴, F. Carnesecchi^{5,19}, R. Caron^{40,85}, J. Castillo Castellanos⁴⁰, E. A. R. Casula⁶², F. Catalano⁶, C. Ceballos Sanchez⁵¹, I. Chakaberia³⁰, P. Chakraborty⁵², S. Chandra¹, S. Chapeland⁵, M. Chartier⁴⁹, S. Chattopadhyay¹, S. Chattopadhyay⁸⁶, T. G. Chavez⁸³, T. Cheng¹⁶, C. Cheshkov⁸⁵, B. Cheynis⁸⁵, V. Chibante Barroso⁵, D. D. Chinellato⁸⁷, S. Cho⁷¹, P. Chochula⁵, P. Christakoglou²⁶, C. H. Christensen⁵⁴, P. Christiansen⁴, T. Chujo⁸⁸, C. Cicalo²², L. Cifarelli¹⁹, F. Cindolo⁷, M. R. Ciupek¹³, G. Clai^{7,149}, J. Cleymans^{89,155}, F. Colamaria⁹⁰, J. S. Colburn⁹¹, D. Colella^{74,75,90}, A. Collu³⁰, M. Colocci^{5,19}, M. Concas^{15,150}, G. Conesa Balbastre⁹², Z. Conesa del Valle³⁴, G. Contin⁷⁶, J. G. Contreras⁶⁴, M. L. Coquet⁴⁰, T. M. Cormier⁷⁰, P. Cortese⁹³, M. R. Cosentino⁹⁴, F. Costa⁵, S. Costanza^{68,69}, P. Crochet⁴⁸, R. Cruz-Torres³⁰, E. Cuautle⁵⁷, P. Cui¹⁶, L. Cunquero⁷⁰, A. Dainese²⁹, M. C. Danisch²⁸, A. Danu⁶⁰, P. Das⁹⁵, P. Das⁴², S. Das⁴², S. Dash⁵², A. De Caro⁹⁶, G. de Cataldo⁹⁰, L. De Cilladi⁵⁸, J. de Cuveland⁹⁷, A. De Falco⁶², D. De Gruttola⁹⁶, N. De Marco¹⁵, C. De Martin⁷⁶, S. De Pasquale⁹⁶, S. Deb³⁸, H. F. Degenhardt⁷³, K. R. Deja⁹⁸, R. Del Grande⁴⁴, L. Dello Stritto⁹⁶, W. Deng¹⁶, P. Dhankher⁹⁹, D. Di Bari⁷⁵, A. Di Mauro⁵, R. A. Diaz¹⁰⁰, T. Dietel⁸⁹, Y. Ding^{16,85}, R. Diviá⁵, D. U. Dixit⁹⁹, Ø. Djuvsland²¹, U. Dmitrieva¹⁰¹, J. Do⁷¹, A. Dobrin⁶⁰, B. Dönigus²³, A. K. Dubey¹, A. Dubla^{13,26}, S. Dudi¹⁰², P. Dupieux⁴⁸, M. Durkac¹⁰³, N. Dzalaiova¹⁰⁴, T. M. Eder²⁷, R. J. Ehlers⁷⁰, V. N. Eikeland²¹, F. Eisenhut²³, D. Elia⁹⁰, B. Erasmus³¹, F. Ercolessi¹⁹, F. Erhardt¹⁰⁵, A. Erokhin²⁴, M. R. Ersdal²¹, B. Espagnon³⁴, G. Eulisse⁵, D. Evans⁹¹, S. Evdokimov¹⁰⁶, L. Fabbietti⁴⁴, M. Faggin⁵⁰, J. Faivre⁹², F. Fan¹⁶, W. Fan³⁰, A. Fantoni⁶³, M. Fasel⁷⁰, P. Fecchio⁶, A. Feliciello¹⁵, G. Feofilov²⁴, A. Fernández Téllez⁸³, A. Ferrero⁴⁰, A. Ferretti⁵⁸, V. J. G. Feuillard²⁸, J. Figiel⁶⁵, V. Filova⁶⁴, D. Finogeev¹⁰¹, F. M. Fionda²², G. Fiorenza⁵, F. Flor²⁰, A. N. Flores⁶⁶, S. Foertsch⁷⁹, S. Fokin¹⁴, E. Fragiaco¹⁰⁷, E. Frajna⁴⁶, A. Francisco⁴⁸, U. Fuchs⁵, N. Funicello⁹⁶, C. Furget⁹², A. Furs¹⁰¹, J. J. Gaardhøje⁵⁴, M. Gagliardi⁵⁸, A. M. Gago⁵³, A. Gal⁵⁵, C. D. Galvan⁸², P. Ganoti⁴⁵, C. Garabatos¹³, J. R. A. Garcia⁸³, E. Garcia-Solis¹⁰⁸, K. Garg³¹, C. Gargiulo⁵, A. Garibli¹⁰⁹, K. Garner²⁷, P. Gasik¹³, E. F. Gauger⁶⁶, A. Gautam⁸¹, M. B. Gay Ducati¹¹⁰, M. Germain³¹, S. K. Ghosh⁴², M. Giacalone¹⁹, P. Gianotti⁶³,

P. J. Steffanic¹¹¹, S. F. Stiefelmaier²⁸, D. Stocco³¹, I. Storehaug³², M. M. Storetvedt¹¹⁹, P. Stratmann²⁷, S. Strazzi¹⁹, C. P. Stylianidis²⁶, A. A. P. Suaide⁷³, C. Suire³⁴, M. Sukhanov¹⁰¹, M. Suljic⁵, R. Sultanov¹², V. Sumberia³⁹, S. Sumowidagdo¹¹, S. Swain¹⁴⁴, A. Szabo¹⁰⁴, I. Szarka¹⁰⁴, U. Tabassam¹⁸, S. F. Taghavi⁴⁴, G. Taillepiepied^{13,48}, J. Takahashi⁸⁷, G. J. Tambave²¹, S. Tang^{16,48}, Z. Tang³⁷, J. D. Tapia Takai^{81,154}, N. Tapus⁸⁴, M. G. Tarzila²⁵, A. Tauro⁵, G. Tejada Muñoz⁸³, A. Telesca⁵, L. Terluzzi⁵⁸, C. Terrevoli²⁰, G. Tersimonov¹⁴⁷, S. Thakur¹, D. Thomas⁶⁶, R. Tieulent⁸⁵, A. Tikhonov¹⁰¹, A. R. Timmins²⁰, M. Tkacik¹⁰³, A. Toia²³, N. Topilskaya¹⁰¹, M. Toppi⁶³, F. Torales-Acosta⁹⁹, T. Tork³⁴, A. G. Torres Ramos⁷⁵, A. Trifiró^{35,137}, A. S. Triolo¹³⁷, S. Tripathy^{7,57}, T. Tripathy⁵², S. Trogolo^{5,50}, V. Trubnikov¹⁴⁷, W. H. Trzaska¹²³, T. P. Trzcinski⁹⁸, A. Tumkin⁷⁷, R. Turrisi²⁹, T. S. Tveter³², K. Ullaland²¹, A. Uras⁸⁵, M. Urioni^{69,72}, G. L. Usai⁶², M. Vala¹⁰, N. Valle⁶⁸, S. Vallerio¹⁵, L. V. R. van Doremalen¹¹⁵, M. van Leeuwen²⁶, R. J. G. van Weelden²⁶, P. Vande Vyvre⁵, D. Varga⁴⁶, Z. Varga⁴⁶, M. Varga-Kofarago⁴⁶, M. Vasileiou⁴⁵, A. Vasiliev¹⁴, O. Vázquez Doce^{44,63}, V. Vechernin²⁴, A. Velure²¹, E. Vercellin⁵⁸, S. Vergara Limón⁸³, L. Vermunt¹¹⁵, R. Vértesi⁴⁶, M. Verweij¹¹⁵, L. Vickovic¹¹⁴, Z. Vilakazi⁸⁰, O. Villalobos Baillie⁹¹, G. Vino⁹⁰, A. Vinogradov¹⁴, T. Virgili⁹⁶, V. Vislavicius⁵⁴, A. Vodopyanov⁵¹, B. Volkel^{5,28}, M. A. Völk¹²⁸, K. Voloshin¹², S. A. Voloshin¹¹³, G. Volpe⁷⁵, B. von Haller⁵, I. Vorobyev⁴⁴, N. Vozniuk¹⁰¹, J. Vrláková¹⁰, B. Wagner²¹, C. Wang¹³⁶, D. Wang¹³⁶, M. Weber⁷⁸, A. Wegrzynek⁵, S. C. Wenzel⁵, J. P. Wessels²⁷, S. L. Weyhmiller³³, J. Wiechula²³, J. Wikne³, G. Wilk¹³³, J. Wilkinson¹³, G. A. Willems²⁷, B. Windelband²⁸, M. Winn⁴⁰, W. E. Witt¹¹¹, J. R. Wright⁶⁶, W. Wu¹³⁶, Y. Wu³⁷, R. Xu¹⁶, A. K. Yadav¹, S. Yalcin¹²⁷, Y. Yamaguchi¹⁴¹, K. Yamakawa¹⁴¹, S. Yang²¹, S. Yano¹⁴¹, Z. Yin¹⁶, I.-K. Yoo¹²⁹, J. H. Yoon⁷¹, S. Yuan²¹, A. Yuncu²⁸, V. Zaccolo⁷⁶, C. Zampolli⁵, H. J. C. Zanoli¹¹⁵, F. Zanone²⁸, N. Zardoshti⁵, A. Zarochentsev²⁴, P. Závada¹⁴⁸, N. Zaviyalov⁷⁷, M. Zhalov⁵⁹, B. Zhang¹⁶, S. Zhang¹³⁶, X. Zhang¹⁶, Y. Zhang³⁷, V. Zhrebchevskii²⁴, Y. Zhi¹³⁵, N. Zhigareva¹², D. Zhou¹⁶, Y. Zhou⁵⁴, J. Zhu^{13,16}, Y. Zhu¹⁶, G. Zinovjev^{147,155} & N. Zurlo^{69,72}

¹Variable Energy Cyclotron Centre, Homi Bhabha National Institute, Kolkata, India. ²Nuclear Physics Institute of the Czech Academy of Sciences, Řež u Prahy, Czech Republic. ³Johann-Wolfgang-Goethe Universität Frankfurt Institut für Informatik, Fachbereich Informatik und Mathematik, Frankfurt, Germany. ⁴Lund University Department of Physics, Division of Particle Physics, Lund, Sweden. ⁵European Organization for Nuclear Research (CERN), Geneva, Switzerland. ⁶Dipartimento DISAT del Politecnico and Sezione INFN, Turin, Italy. ⁷INFN, Sezione di Bologna, Bologna, Italy. ⁸Department of Physics, Aligarh Muslim University, Aligarh, India. ⁹Korea Institute of Science and Technology Information, Daejeon, Republic of Korea. ¹⁰Faculty of Science, P.J. Šafarik University, Košice, Slovakia. ¹¹Indonesian Institute of Sciences, Jakarta, Indonesia. ¹²NRC Kurchatov Institute—ITEP, Moscow, Russia. ¹³Research Division and ExtreMe Matter Institute EMMI, GSI Helmholtzzentrum für Schwerionenforschung GmbH, Darmstadt, Germany. ¹⁴National Research Centre Kurchatov Institute, Moscow, Russia. ¹⁵INFN, Sezione di Torino, Turin, Italy. ¹⁶Central China Normal University, Wuhan, China. ¹⁷Instituto de Física, Universidad Nacional Autónoma de México, México City, México. ¹⁸COMSATS University Islamabad, Islamabad, Pakistan. ¹⁹Dipartimento di Fisica e Astronomia dell'Università and Sezione INFN, Bologna, Italy. ²⁰University of Houston, Houston, TX, USA. ²¹Department of Physics and Technology, University of Bergen, Bergen, Norway. ²²INFN, Sezione di Cagliari, Cagliari, Italy. ²³Institut für Kernphysik, Johann Wolfgang Goethe-Universität Frankfurt, Frankfurt, Germany. ²⁴St Petersburg State University, St Petersburg, Russia. ²⁵Horia Hulubei National Institute of Physics and Nuclear Engineering, Bucharest, Romania. ²⁶Nikhef, National Institute for Subatomic Physics, Amsterdam, Netherlands. ²⁷Westfälische Wilhelms-Universität Münster, Institut für Kernphysik, Münster, Germany. ²⁸Physikalisches Institut, Ruprecht-Karls-Universität Heidelberg, Heidelberg, Germany. ²⁹INFN, Sezione di Padova, Padova, Italy. ³⁰Lawrence Berkeley National Laboratory, Berkeley, California, USA. ³¹SUBATECH, IMT Atlantique, Université de Nantes, CNRS-IN2P3, Nantes, France. ³²Department of Physics, University of Oslo, Oslo, Norway. ³³Yale University, New Haven, CT, USA. ³⁴Laboratoire de Physique des 2 Infinis, Irene Joliot-Curie, Orsay, France. ³⁵INFN, Sezione di Catania, Catania, Italy. ³⁶Gangneung-Wonju National University, Gangneung, Republic of Korea. ³⁷University of Science and Technology of China, Hefei, China. ³⁸Indian Institute of Technology Indore, Indore, India. ³⁹Physics Department, University of Jammu, Jammu, India. ⁴⁰Université Paris-Saclay Centre d'Études de Saclay (CEA), IRFU, Département de Physique Nucleaire (DPHn), Saclay, France. ⁴¹AGH University of Science and Technology, Cracow, Poland. ⁴²Bose Institute, Department of Physics and Centre for Astroparticle Physics and Space Science (CAPSS), Kolkata, India. ⁴³Dipartimento di Fisica e Astronomia dell'Università and Sezione INFN, Catania, Italy. ⁴⁴Physik Department, Technische Universität München, Munich, Germany. ⁴⁵National and Kapodistrian University of Athens, School of Science, Department of Physics, Athens, Greece. ⁴⁶Wigner Research Centre for Physics, Budapest, Hungary. ⁴⁷Nuclear Physics Group, STFC Daresbury Laboratory, Daresbury, UK. ⁴⁸Université Clermont Auvergne, CNRS/IN2P3, LPC, Clermont-Ferrand, France. ⁴⁹University of Liverpool, Liverpool, UK. ⁵⁰Dipartimento di Fisica e Astronomia dell'Università and Sezione INFN, Padova, Italy. ⁵¹Joint Institute for Nuclear Research (JINR), Dubna, Russia. ⁵²Indian Institute of Technology (IIT) Bombay, Mumbai, India. ⁵³Sección Física, Departamento de Ciencias, Pontificia Universidad Católica del Perú, Lima, Perú. ⁵⁴Niels Bohr Institute, University of Copenhagen, Copenhagen, Denmark. ⁵⁵Université de Strasbourg, CNRS, IPHC UMR 7178, Strasbourg, France. ⁵⁶NRNU Moscow Engineering Physics Institute, Moscow, Russia. ⁵⁷Instituto de Ciencias Nucleares, Universidad Nacional Autónoma de México, México City, México. ⁵⁸Dipartimento di Fisica dell'Università and Sezione INFN, Turin, Italy. ⁵⁹Petersburg Nuclear Physics Institute, Gatchina, Russia. ⁶⁰Institute of Space Science (ISS), Bucharest, Romania. ⁶¹Gauhati University, Department of Physics, Guwahati, India. ⁶²Dipartimento di Fisica dell'Università and Sezione INFN, Cagliari, Italy. ⁶³INFN, Laboratori Nazionali di Frascati, Frascati, Italy. ⁶⁴Faculty of Nuclear Sciences and Physical Engineering, Czech Technical University in Prague, Prague, Czech Republic. ⁶⁵The Henryk Niewodniczanski Institute of Nuclear Physics, Polish Academy of Sciences, Cracow, Poland. ⁶⁶The University of Texas at Austin, Austin, TX, USA. ⁶⁷Moscow Institute for Physics and Technology, Moscow, Russia. ⁶⁸Dipartimento di Fisica e Nucleare e Teorica, Università di Pavia, Pavia, Italy. ⁶⁹INFN, Sezione di Pavia, Pavia, Italy. ⁷⁰Oak Ridge National Laboratory, Oak Ridge, TN, USA. ⁷¹Inha University, Incheon, Republic of Korea. ⁷²Università di Brescia, Brescia, Italy. ⁷³Universidade de Sao Paulo (USP), Sao Paulo, Brazil. ⁷⁴Politecnico di Bari and Sezione INFN, Bari, Italy. ⁷⁵Dipartimento Interateneo di Fisica 'M. Merlin' and Sezione INFN, Bari, Italy. ⁷⁶Dipartimento di Fisica dell'Università and Sezione INFN, Trieste, Italy. ⁷⁷Russian Federal Nuclear Center (VNIIEF), Sarov, Russia. ⁷⁸Stefan Meyer Institut für Subatomare Physik (SMI), Vienna, Austria. ⁷⁹iThemba LABS, National Research Foundation, Somerset West, South Africa. ⁸⁰University of the Witwatersrand, Johannesburg, South Africa. ⁸¹University of Kansas, Lawrence, KS, USA. ⁸²Universidad Autónoma de Sinaloa, Culiacan, Mexico. ⁸³High Energy Physics Group, Universidad Autónoma de Puebla, Puebla, Mexico. ⁸⁴University Politehnica of Bucharest, Bucharest, Romania. ⁸⁵Université de Lyon, CNRS/IN2P3, Institut de Physique des 2 Infinis de Lyon, Lyon, France. ⁸⁶Saha Institute of Nuclear Physics, Homi Bhabha National Institute, Kolkata, India. ⁸⁷Universidade Estadual de Campinas (UNICAMP), Campinas, Brazil. ⁸⁸University of Tsukuba, Tsukuba, Japan. ⁸⁹University of Cape Town, Cape Town, South Africa. ⁹⁰INFN, Sezione di Bari, Bari, Italy. ⁹¹School of Physics and Astronomy, University of Birmingham, Birmingham, UK. ⁹²Laboratoire de Physique Subatomique et de Cosmologie, Université Grenoble-Alpes, CNRS-IN2P3, Grenoble, France. ⁹³Dipartimento di Scienze e Innovazione Tecnologica dell'Università del Piemonte Orientale and INFN Sezione di Torino, Alessandria, Italy. ⁹⁴Universidade Federal do ABC, Santo André, Brazil. ⁹⁵National Institute of Science Education and Research, Homi Bhabha National Institute, Jatni, India. ⁹⁶Dipartimento di Fisica 'E.R. Caianiello'

dell'Universita and Gruppo Collegato INFN, Salerno, Italy. ⁹⁷Frankfurt Institute for Advanced Studies, Johann Wolfgang Goethe-Universität Frankfurt, Frankfurt, Germany. ⁹⁸Warsaw University of Technology, Warsaw, Poland. ⁹⁹Department of Physics, University of California, Berkeley, Berkeley, CA, USA. ¹⁰⁰Centro de Aplicaciones Tecnológicas y Desarrollo Nuclear (CEADEN), Havana, Cuba. ¹⁰¹Institute for Nuclear Research, Academy of Sciences, Moscow, Russia. ¹⁰²Physics Department, Panjab University, Chandigarh, India. ¹⁰³Technical University of Košice, Košice, Slovakia. ¹⁰⁴Comenius University Bratislava, Faculty of Mathematics, Physics and Informatics, Bratislava, Slovakia. ¹⁰⁵Physics Department, Faculty of Science, University of Zagreb, Zagreb, Croatia. ¹⁰⁶NRC Kurchatov Institute IHEP, Protvino, Russia. ¹⁰⁷INFN, Sezione di Trieste, Trieste, Italy. ¹⁰⁸Chicago State University, Chicago, IL, USA. ¹⁰⁹National Nuclear Research Center, Baku, Azerbaijan. ¹¹⁰Instituto de Física, Universidade Federal do Rio Grande do Sul (UFRGS), Porto Alegre, Brazil. ¹¹¹University of Tennessee, Knoxville, TN, USA. ¹¹²Nagasaki Institute of Applied Science, Nagasaki, Japan. ¹¹³Wayne State University, Detroit, MI, USA. ¹¹⁴Faculty of Electrical Engineering, Mechanical Engineering and Naval Architecture, University of Split, Split, Croatia. ¹¹⁵Institute for Gravitational and Subatomic Physics (GRASP), Utrecht University/Nikhef, Utrecht, Netherlands. ¹¹⁶A.I. Alikhanyan National Science Laboratory (Yerevan Physics Institute) Foundation, Yerevan, Armenia. ¹¹⁷University of Tokyo, Tokyo, Japan. ¹¹⁸Helmholtz-Institut für Strahlen- und Kernphysik, Rheinische Friedrich-Wilhelms-Universität Bonn, Bonn, Germany. ¹¹⁹Faculty of Engineering and Science, Western Norway University of Applied Sciences, Bergen, Norway. ¹²⁰Centro de Investigación y de Estudios Avanzados (CINVESTAV), Mexico City and Merida, Mexico. ¹²¹Yonsei University, Seoul, Republic of Korea. ¹²²Creighton University, Omaha, NW, USA. ¹²³University of Jyväskylä, Jyväskylä, Finland. ¹²⁴Ohio State University, Columbus, OH, USA. ¹²⁵Suranaree University of Technology, Nakhon Ratchasima, Thailand. ¹²⁶Institute of Experimental Physics, Slovak Academy of Sciences, Košice, Slovakia. ¹²⁷KTO Karatay University, Konya, Turkey. ¹²⁸Hochschule Worms, Zentrum für Technologietransfer und Telekommunikation (ZTT), Worms, Germany. ¹²⁹Department of Physics, Pusan National University, Pusan, Republic of Korea. ¹³⁰Jeonbuk National University, Jeonju, Republic of Korea. ¹³¹Department of Physics, Sejong University, Seoul, Republic of Korea. ¹³²California Polytechnic State University, San Luis Obispo, California, USA. ¹³³National Centre for Nuclear Research, Warsaw, Poland. ¹³⁴University of South-Eastern Norway, Tonsberg, Norway. ¹³⁵China Institute of Atomic Energy, Beijing, China. ¹³⁶Fudan University, Shanghai, China. ¹³⁷Dipartimento di Scienze MIFT, Università di Messina, Messina, Italy. ¹³⁸Università degli Studi di Foggia, Foggia, Italy. ¹³⁹Helsinki Institute of Physics (HIP), Helsinki, Finland. ¹⁴⁰Chungbuk National University, Cheongju, Republic of Korea. ¹⁴¹Hiroshima University, Hiroshima, Japan. ¹⁴²Budker Institute for Nuclear Physics, Novosibirsk, Russia. ¹⁴³Physics Department, University of Rajasthan, Jaipur, India. ¹⁴⁴Institute of Physics, Homi Bhabha National Institute, Bhubaneswar, India. ¹⁴⁵Physikalisches Institut, Eberhard-Karls-Universität Tübingen, Tübingen, Germany. ¹⁴⁶Nara Women's University (NWU), Nara, Japan. ¹⁴⁷Bogolyubov Institute for Theoretical Physics, National Academy of Sciences of Ukraine, Kiev, Ukraine. ¹⁴⁸Institute of Physics of the Czech Academy of Sciences, Prague, Czech Republic. ¹⁴⁹Present address: Italian National Agency for New Technologies, Energy and Sustainable Economic Development (ENEA), Bologna, Italy. ¹⁵⁰Present address: Dipartimento DET del Politecnico di Torino, Turin, Italy. ¹⁵¹Present address: M.V. Lomonosov Moscow State University, D.V. Skobel'syn Institute of Nuclear Physics, Moscow, Russia. ¹⁵²Present address: Department of Applied Physics, Aligarh Muslim University, Aligarh, India. ¹⁵³Present address: Institute of Theoretical Physics, University of Wrocław, Warsaw, Poland. ¹⁵⁴Present address: University of Kansas, Lawrence, KS, USA. ¹⁵⁵Deceased: J. Cleymans, G. Zinovjev. ✉e-mail: alice-publications@cern.ch

Methods

Event selection

The inelastic pp and Pb–Pb events were recorded with the ALICE apparatus at collision energies of $\sqrt{s} = 13$ TeV and $\sqrt{s_{NN}} = 5.02$ TeV, respectively. Events are triggered by the V0 detector comprising two plastic scintillator arrays placed on both sides of the interaction point and covering the pseudorapidity intervals of $2.8 < \eta < 5.1$ and $-3.7 < \eta < -1.7$. The pseudorapidity is defined as $\eta = -\ln \left[\tan \left(\frac{\Theta}{2} \right) \right]$, where Θ is the polar angle of the particle with respect to the beam axis. The trigger condition is defined by the coincidence of signals in both arrays of the V0 detector. Together with the two innermost layers of the ITS detector, V0 is also used to reject background events like beam–gas interactions or collisions with mechanical structures of the beamline. For the analysis of pp data, a high-multiplicity trigger is employed to select only events with the total signal amplitude measured in the V0 detector above a certain threshold, which leads to a selection of about 0.17% of the inelastic pp collisions with the highest V0 signal. In these events, the number of charged particles produced at midrapidity $|\eta| < 0.5$ is about six times higher than $\langle dN_{ch}/dy \rangle = 5.31 \pm 0.18$ measured in inelastic pp collisions at $\sqrt{s} = 13$ TeV (ref. ⁸⁰). This facilitates the analysis of rarely produced (anti)³He nuclei. As for the Pb–Pb experimental data, 10% of all inelastic events with the highest signal amplitude in the V0 detector are considered for the analysis. In these events, the average charged-particle multiplicity at midrapidity $|\eta| < 0.5$ amounts to $\langle dN_{ch}/dy \rangle = 1,764 \pm 50$ (ref. ⁸¹). In total, 147.9×10^6 Pb–Pb and 10^9 pp events were analysed.

Particle tracking and identification

Trajectories of charged particles are reconstructed in the ALICE central barrel from their hits in the ITS and TPC. The detectors are located inside a solenoidal magnetic field (0.5 T) bending the trajectories of charged particles. The curvature and direction of the charged-particle trajectories in the magnetic field are used to reconstruct their momentum. The detectors provide full azimuthal coverage in the pseudorapidity interval $|\eta| < 0.9$. This η range corresponds to the region within $\pm 42^\circ$ of the transverse plane that is perpendicular to the beam axis. Typical resolution of the transverse momentum reconstructed at the primary vertex ($p_{T,primary}$) for protons, pions and kaons varies from about 2% for tracks with $p_{T,primary} = 10$ GeV c^{-1} to below 1% for $p_{T,primary} \leq 1$ GeV c^{-1} .

Specific energy loss in the TPC gas is used to identify charged particles. Due to their electric charge ($z = 2$), high mass and quadratic dependence of specific energy loss on particle charge, ³He and ³He nuclei have larger energy loss than most other (anti)particles produced in collisions (like pions, kaons, protons and deuterons) and can be clearly identified in the TPC. The selected ³He candidates include a substantial amount of background from secondary nuclei that originate from spallation reactions in the detector material and can be seen at low momentum (Fig. 1b). This contribution is estimated via a fit to the distribution of the measured distance of closest approach between the track candidates and the primary collision vertex using templates from MC simulations. Since primary particles point back to the primary vertex, they are characterized by a distinct peak structure at zero distance of closest approach, whereas secondary particles correspond to a flat distribution of the distance of closest approach and their contribution can, therefore, be separated. More details on this procedure can be found elsewhere^{12,47}. For ³He candidates in pp collisions at $\sqrt{s} = 13$ TeV, this contribution amounts to $\sim 75\%$ in the lowest analysed momentum interval of $0.65 \leq p_{primary}/z < 0.80$ GeV c^{-1} and is negligible in the momentum range above $p_{primary}/z = 1.50$ GeV c^{-1} . For ³He nuclei, there is no contribution from spallation processes. In total, there are $16,801 \pm 130$ primary ³He reconstructed in the TPC in the Pb–Pb data sample. In the sample of pp collisions, the total number of reconstructed primary candidates of ³He and ³He is 773 ± 46 and 652 ± 30 , respectively. The uncertainties for these values result from the fit to the TPC signal, which is used to reject the (small) background from (anti)triton nuclei misidentified as (anti)³He at low momenta.

Corrections and evaluation of systematic uncertainties

Due to continuous energy-loss effects in the detector material, the inelastic interaction of ³He with the detector material happens at momentum p , which is lower than momentum $p_{primary}$ reconstructed at the primary collision vertex. The corresponding effect is taken into account utilizing MC simulations in which one has precise information about both momenta for each (anti)particle. In the analysis of pp collisions, the average values of $p/p_{primary}$ distributions in each analysed $p_{primary}$ interval are used to consider the energy loss. The root mean square (r.m.s.) value of these distributions is used to determine the uncertainty in momentum p , which is propagated to the uncertainty of the measured cross section. For the analysis of the Pb–Pb data sample, the MC information on the momenta of daughter tracks originating from ³He annihilation is used to estimate the corresponding effect and resulting uncertainty.

The systematic uncertainties due to tracking, particle identification and description of material budget in MC simulations are considered, and the total uncertainty is obtained as the quadratic sum of the individual contributions. The material budget of the ALICE apparatus^{50,82,82} is varied by $\pm 4.5\%$ in MC simulations, and the deviations in the final results from the default case are considered as an uncertainty. The precision of $\sim 4.5\%$ of the MC parameterization is validated for the ALICE material with photon conversion analyses (up to the outer TPC vessel⁵⁰) and with tagged pion and proton absorption studies (for the material between TPC and TOF detectors⁵²).

For the Pb–Pb analysis, the total systematic uncertainty amounts to $\sim 20\%$ in the highest and lowest momentum intervals considered in the analysis and decreases to $\leq 10\%$ in the momentum interval of $3 \leq p < 7$ GeV c^{-1} . For the analysis of pp data (which is based on the antibaryon-to-baryon ratio method), an additional uncertainty due to primordial antibaryon-to-baryon ratio produced in collisions is considered as a global uncertainty. The primordial antiproton-to-proton ratio of 0.998 ± 0.015 is extrapolated for the $\sqrt{s} = 13$ TeV collision energy from available measurements^{47,51}; furthermore, under the assumption that the (anti)³He yield is proportional to the cube of the (anti)proton yield⁴², the primary ³He/³He ratio amounts to 0.994 ± 0.045 . This uncertainty is the dominant contribution to the total systematic uncertainty for the pp analysis, which amounts to $\sim 8\%$.

MC simulation

The results presented in this Article are compared with the detailed MC simulations of the ALICE detector. The simulations start with the generation of (anti)particles at the primary collision vertex and the production of raw detector information, also taking into account inactive subdetector channels. The same reconstruction algorithms applied to real experimental data are employed to analyse the raw simulated data. For the pp analysis based on the antimatter-to-matter ratio, the primordial ³He/³He ratio of 0.994 is used as an input for the MC simulations. Since the average multiplicity in pp collisions at midrapidity is low, no underlying event was simulated in this case. For the TOF-to-TPC analysis in Pb–Pb collisions, the simulations contain an underlying Pb–Pb event that was generated with the help of the HIJING event generator^{83–85}. On top of this underlying event, 160 nuclei of ³He were injected following the momentum distribution obtained from independent studies on ³He production¹².

For the propagation of (anti)particles through the detector material, the simulations rely on the Geant4 software package⁵³, in which the inelastic cross section of ³He nuclei is based on Glauber calculations. Since the Glauber model simulations are computationally too expensive to be performed during the propagation steps through the material, they are parameterized as a function of atomic mass number A of the target nucleus⁵⁴:

$$\sigma_{hA}^{inel} = \pi R_A^2 \ln \left(1 + \frac{A \sigma_{hN}^{tot}}{\pi R_A^2} \right). \quad (1)$$

Here h denotes the nucleus in question ($h = \bar{p}, \bar{d}, {}^3\bar{\text{He}}$ and ${}^4\bar{\text{He}}$) and A is the atomic number of the target nucleus with radius R_A . Also, σ_{hN}^{tot} is the total (elastic plus inelastic) cross section of hadron h on nucleon N , which is estimated with the help of Glauber calculations by extrapolating the measured $\bar{p}p$ values⁵⁶ to larger antinuclei. We performed several full-scale MC simulations with varied inelastic cross sections of ${}^3\bar{\text{He}}$ with matter, and the simulated observables used in this analysis are studied as a function of the inelastic cross-section re-scaling. This dependence is parameterized using the Lambert–Beer law (Fig. 1e,f). The parameterization reads as $N_{\text{surv}} = N_0 \times \exp(-\sigma_{\text{inel}}\rho L)$, where N_0 corresponds to the number of incident particles, N_{surv} is the number of survived particles that did not get absorbed, σ_{inel} is the inelastic cross section, ρ is the density of the material crossed and L is the length of the particle trajectory in the material. The free parameter given by the product ρL is determined by a fit to the simulated observables.

To model the inelastic cross section of ${}^3\bar{\text{He}}$ nuclei in the interstellar medium, the Geant4 parameterization of the ${}^3\bar{\text{He}}-p$ inelastic cross section is scaled with the correction factors obtained from the ALICE measurements. The additional uncertainty that originates from re-scaling a measurement at $\langle A \rangle = 17.4$ and $\langle A \rangle = 34.7$ to $A = 1$ and $A = 4$ is taken from the difference between the parameterization for the dependence on A in Geant4 and in full Glauber calculation and amounts to $<8\%$ (ref. 54). The resulting ${}^3\bar{\text{He}}-p$ inelastic cross section is shown in Extended Data Fig. 1 (left) together with the model employed in another work³⁰. The latter is based on the approximation that uses available measurements to estimate the inelastic antideuteron–proton cross section in the following way:

$$\sigma_{\text{inel}}^{\bar{d}p} \approx \frac{\sigma_{\text{tot}}^{\bar{d}p}}{\sigma_{\text{tot}}^{\bar{p}p}} (\sigma_{\text{tot}}^{\bar{p}p} - \sigma_{\text{el}}^{\bar{p}p}). \quad (2)$$

By symmetry, the total antideuteron–proton cross section $\sigma_{\text{tot}}^{\bar{d}p}$ is equal to the total deuteron–antiproton cross section taken from elsewhere⁸⁶. For antihelium, the inelastic cross section is scaled from antideuterons according to the mass number as $\sigma_{\text{inel}}^{{}^3\bar{\text{He}}p} = \frac{3}{2} \sigma_{\text{inel}}^{\bar{d}p}$. Extended Data Fig. 1 (right) also shows the resulting ${}^3\bar{\text{He}}-{}^4\text{He}$ inelastic cross section obtained in the same way for the ${}^4\text{He}$ target.

The results for the inelastic ${}^3\bar{\text{He}}$ cross section are also tested against the modifications of elastic cross sections of ${}^3\bar{\text{He}}$ nuclei. Both ${}^3\text{He}$ and ${}^3\bar{\text{He}}$ elastic cross sections are independently varied by 30%, which led to $\leq 1\%$ modifications of the final results. For the analysis of proton–proton collisions based on the antibaryon-to-baryon ratio method, the results are additionally investigated for the sensitivity to the ${}^3\text{He}$ inelastic cross section. The latter is varied by 10%, which is the uncertainty of the Geant4 parameterizations obtained from fits to the experimental data⁸⁷. This variation yields a modification of $\leq 2.3\%$ in the reconstructed antihelium-to-helium ratio.

Propagation modelling

The possible sources of antinuclei in our Galaxy are either cosmic-ray interactions with nuclei in the interstellar gas or more exotic sources such as DM annihilations or decays. Cosmic rays mainly consist of protons and originate from supernovae remnants, whereas DM has so far escaped direct or indirect detection but its density profile can be modelled⁸⁸.

The propagation in the Galaxy can be carried out using the publicly available propagation models^{63–66}. We choose the GALPROP code (version 56 available at <https://galprop.stanford.edu>) for the implementation of ${}^3\bar{\text{He}}$ cosmic-ray propagation, which is discussed in detail elsewhere⁸⁹. GALPROP numerically solves a general transport equation for all the included particle species⁶⁶. This transport equation reads as

$$\frac{\partial \psi}{\partial t} = q(\mathbf{r}, p) + \nabla \cdot (D_{xx} \mathbf{grad} \psi - \mathbf{V} \psi) + \frac{\partial}{\partial p} p^2 D_{pp} \frac{\partial \psi}{\partial p} - \frac{\partial}{\partial p} \left[\psi \frac{dp}{dt} - \frac{p}{3} (\nabla \cdot \mathbf{V}) \psi \right] - \frac{\psi}{\tau}. \quad (3)$$

Here $\psi = \psi(\mathbf{r}, p, t)$ is the time-dependent ${}^3\bar{\text{He}}$ density per unit of the total particle momentum and $q(\mathbf{r}, p)$ is the source function for ${}^3\bar{\text{He}}$. The second and third terms describe the propagation of ${}^3\bar{\text{He}}$, where D_{xx} , \mathbf{V} and D_{pp} are the spatial diffusion coefficient, convection velocity and diffusive re-acceleration coefficient, respectively. Although the effect of the Galactic magnetic field is not explicitly modelled, it is accounted for by these terms of the transport equation. These coefficients are the same for all the particle species and can be constrained using available cosmic-ray measurements. We use the best-fit values of these parameters provided elsewhere⁴⁶. The fourth term accounts for momentum losses via cosmic-ray interactions with interstellar gas (dp/dt) and adiabatic momentum losses ($\nabla \cdot \mathbf{V}$). The last term represents the ${}^3\bar{\text{He}}$ inelastic collisions with interstellar gas, where $1/\tau$ is the fragmentation rate. It is related to the inelastic cross section as follows:

$$\frac{1}{\tau} = \beta c \left(n_{\text{H}}(\mathbf{r}) \sigma_{\text{inel}}^{{}^3\bar{\text{He}}p}(p) + n_{\text{He}}(\mathbf{r}) \sigma_{\text{inel}}^{{}^3\bar{\text{He}}{}^4\text{He}}(p) \right). \quad (4)$$

The elastic re-scattering of cosmic-ray antinuclei in the interstellar medium is assumed to have a negligible effect on diffusive propagation⁹⁰. The second and third terms in equation (3) can cause both acceleration and deceleration, which means that the final flux at a given energy also depends on the initial fluxes at both higher and lower energies. Therefore, the final number of particles in a specific energy interval depends on (i) the energy spectrum and spatial distribution of the source, (2) propagation parameters, (3) particles' momentum loss/gain and (4) annihilation cross section. Only the first and last terms of equation (3) require particle-specific information. Here ${}^3\bar{\text{He}}$ nuclei can be produced when cosmic-ray particles interact with protons or ${}^4\text{He}$ nuclei in the interstellar medium. The ${}^3\bar{\text{He}}$ source function in this case is

$$q(\mathbf{r}, p) = \sum_{\text{CR}=\text{H,He}} \sum_{\text{ISM}=\text{H,He}} n_{\text{ISM}}(\mathbf{r}) \int dp'_{\text{CR}} \beta_{\text{CR}} c \frac{d\sigma(p, p'_{\text{CR}})}{dp} n_{\text{CR}}(\mathbf{r}, p'_{\text{CR}}). \quad (5)$$

The density of hydrogen and helium gas is represented by $n_{\text{ISM}}(\mathbf{r})$, and p'_{CR} , β_{CR} and $n_{\text{CR}}(\mathbf{r}, p'_{\text{CR}})$ are the momentum, velocity and density of cosmic rays, respectively, whereas p is the momentum of the produced ${}^3\bar{\text{He}}$. Also, $d\sigma(p, p'_{\text{CR}})/dp$ is the ${}^3\bar{\text{He}}$ differential production cross section for the specific collision and includes primary ${}^3\bar{\text{He}}$ as well as the products of \bar{t} decays. The most abundant cosmic rays are protons and helium; thus, this source function must be calculated for both species and summed up. In another work⁵⁷, all the relevant types of collision between protons and ${}^4\text{He}$ nuclei with projectile beam energies ranging from 31.0 GeV to 12.5 TeV are considered, and the so-called spherical approximation is used in which antinucleons with a momentum difference smaller than p_0 are forming an antinucleus^{57,91}. The parameter p_0 depends on the collision energy and is constrained by several accelerator-based measurements^{1–17}, including measurements at the LHC^{92,93}. The resulting injection spectra obtained from the collisions of cosmic rays with the interstellar medium peak above $7 \text{ GeV} A^{-1}$ (ref. 57).

In the case of ${}^3\bar{\text{He}}$ nuclei produced from DM annihilations, the source function depends on the thermally averaged annihilation cross section times the velocity ($\langle \sigma v \rangle$), density (ρ_{DM}) of the DM, mass (m_χ) of the DM particle and the resulting ${}^3\bar{\text{He}}$ spectrum (dN/dE_{kin}) (ref. 29):

$$q(\mathbf{r}, E_{\text{kin}}) = \frac{1}{2} \frac{\rho_{\text{DM}}^2(\mathbf{r})}{m_\chi^2} \langle \sigma v \rangle \frac{dN}{dE_{\text{kin}}}. \quad (6)$$

Here E_{kin} is the kinetic energy of the produced ${}^3\bar{\text{He}}$ including those that are the products of \bar{t} decays. The spectrum is calculated utilizing the PYTHIA 8.156 event generator⁹⁴ and a coalescence model with a coalescence momentum $p_0 = 357 \text{ MeV} c^{-1}$, as described in more detail elsewhere²⁹. We set $\langle \sigma v \rangle = 2.6 \times 10^{-26} \text{ cm}^3 \text{ s}^{-1}$ (ref. 30). We implemented

the Navarro–Frenk–White profile in GALPROP, which is one of the most commonly used DM density profiles:

$$\rho(r) = \frac{\rho_0}{\frac{r}{R_s} \left(1 + \frac{r}{R_s}\right)^2}. \quad (7)$$

Here r is the distance to the Galactic Centre, ρ_0 is an overall normalization such that $\rho(r)$ is equal to the local density $\rho_\odot = 0.39 \text{ GeV cm}^{-3}$ at $r = 8.5 \text{ kpc}$ and $R_s = 24.42 \text{ kpc}$ is a scale radius²⁹. In contrast to the spectra of ${}^3\text{He}$ from collisions of cosmic rays with the interstellar medium, the resulting spectrum for ${}^3\text{He}$ originating from DM annihilation peaks at low kinetic energies of around $0.1 \text{ GeV } A^{-1}$ (ref. 29).

Discussion of uncertainties on ${}^3\text{He}$ cosmic-ray modelling

The results presented in this paper focus on the impact of ALICE measurements for $\sigma_{\text{inel}}({}^3\text{He})$ on the cosmic-ray ${}^3\text{He}$ flux and the corresponding transparency of the Galaxy. To this purpose, we have considered two models of ${}^3\text{He}$ sources described in the main text and only propagated the uncertainty of the $\sigma_{\text{inel}}({}^3\text{He})$ measurement. Here we briefly discuss other possible uncertainties related to the ${}^3\text{He}$ cosmic-ray modelling.

As for the DM source, it is apparent that a different DM mass assumption changes the antinuclei flux profile near Earth^{22,29,31}. The DM mass assumptions around $m_\chi \approx 100 \text{ GeV}$ are favoured by recent AMS-02 antiproton data³¹, for very different values of m_χ , the ${}^3\text{He}$ flux and the corresponding transparency can be studied as described in this work. Variation in the DM annihilation cross section $\langle\sigma v\rangle$ leads to a constant scaling of ${}^3\text{He}$ flux according to equation (6) and therefore to identical transparency values. Although the Navarro–Frenk–White profile is used in this work to describe the distribution of DM in the Galaxy, other profiles are also available such as Einasto²², Burkert⁹⁵ or the isothermal one⁹⁶. Antiproton limits on $\langle\sigma v\rangle$ are partially degenerate with the effect of different DM profiles, and the overall impact of varying the DM profiles on the maximum allowed antinuclei flux is minor^{30,61}. If the isothermal profile is employed instead of the Navarro–Frenk–White one, the obtained ${}^3\text{He}$ transparency is shifted up by 10%–15%.

Although coalescence-based models can successfully describe antinuclei production, the model uncertainties are still relatively large, which leads to substantial changes in the magnitude of antinuclei fluxes^{22,30,61}. In general, as long as different coalescence models retain the shape of the produced antinuclei momentum spectrum, the resulting transparency is not affected. For example, the change in coalescence parameter p_0 leads to constant scaling of the antinuclei flux and identical transparency values.

The GALPROP parameters used in this work are tuned to reproduce the available experimental data on cosmic-ray nuclei (up to $Z = 28$). The obtained uncertainties on the nuclei fluxes of $\lesssim 10\%$ (ref. 46) are not considered in this work, since they result in a negligible change in ${}^3\text{He}$ fluxes. An alternative set of propagation parameters has been obtained⁷⁸ by considering a subsample of the available cosmic-ray data. The comparison between the two sets is discussed in more details elsewhere⁶¹. The employment of these alternative parameters decreases the ${}^3\text{He}$ background flux by one order of magnitude at the lowest E_{kin} value considered in this work and results in about 60% lower transparency. For the DM signal, the corresponding flux is up to a factor of five higher at the lowest E_{kin} value with about 40% lower transparency. These differences in fluxes and transparencies are obtained before the solar modulation and become minor for $E_{\text{kin}} \gtrsim 10 \text{ GeV } A^{-1}$, for the DM signal as well as the background.

Data availability

All the data shown in the histograms and plots are publicly available via the HEPData repository at <https://www.hepdata.net/record/ins2026264>.

Code availability

The source code utilized in this study is publicly available under the names AliPhysics (<https://github.com/alisw/AliPhysics>) and AliRoot (<https://github.com/alisw/AliRoot>). The source code for the propagation of antinuclei is publicly available under the name Galprop (<https://galprop.stanford.edu/>, v56). Specific modifications of the Galprop source code used in this work are publicly available in the AliPhysics repository. Further information can be provided by the corresponding author upon reasonable request.

References

- ALICE Collaboration et al. Pseudorapidity and transverse-momentum distributions of charged particles in proton–proton collisions at $\sqrt{s}=13 \text{ TeV}$. *Phys. Lett. B* **753**, 319–329 (2016).
- ALICE Collaboration et al. Centrality dependence of the charged-particle multiplicity density at midrapidity in Pb–Pb collisions at $\sqrt{s_{\text{NN}}}=5.02 \text{ TeV}$. *Phys. Rev. Lett.* **116**, 222302 (2016).
- ALICE Collaboration et al. Measurement of the low-energy antideuteron inelastic cross section. *Phys. Rev. Lett.* **125**, 162001 (2020).
- Wang, X.-N. & Gyulassy, M. HIJING: a Monte Carlo model for multiple jet production in pp, pA and AA collisions. *Phys. Rev. D* **44**, 3501–3516 (1991).
- ALICE Collaboration et al. ALICE: physics performance report, volume II. *J. Phys. G* **32**, 1295–2040 (2006).
- ALICE Collaboration et al. Centrality dependence of the charged-particle multiplicity density at mid-rapidity in Pb–Pb collisions at $\sqrt{s_{\text{NN}}}=2.76 \text{ TeV}$. *Phys. Rev. Lett.* **106**, 032301 (2011).
- Particle Data Group Collaboration et al. Review of particle physics. *PTEP* **2020**, 083C01 (2020).
- Ingemarsson, A. et al. Reaction cross sections of intermediate energy ${}^3\text{He}$ -particles on targets from ${}^9\text{Be}$ to ${}^{208}\text{Pb}$. *Nucl. Phys. A* **696**, 3–30 (2001).
- Lin, H.-N. & Li, X. The dark matter profiles in the Milky Way. *Mon. Not. R. Astron. Soc.* **487**, 5679–5684 (2019).
- ALICE Collaboration. Modelling of antihelium-3 cosmic-ray propagation. ALICE-PUBLIC-2022-002 (2022).
- Duperray, R. et al. Flux of light antimatter nuclei near Earth, induced by cosmic rays in the Galaxy and in the atmosphere. *Phys. Rev. D* **71**, 083013 (2005).
- Gomez-Coral, D.-M. et al. Deuteron and antideuteron production simulation in cosmic-ray interactions. *Phys. Rev. D* **98**, 023012 (2018).
- ALICE Collaboration et al. Production of deuterons, tritons, ${}^3\text{He}$ nuclei and their antinuclei in pp collisions at $\sqrt{s}=0.9, 2.76$ and 7 TeV . *Phys. Rev.* **C97**, 024615 (2018).
- ALICE Collaboration et al. (Anti-)deuteron production in pp collisions at $\sqrt{s}=13 \text{ TeV}$. *Eur. Phys. J. C* **80**, 889 (2020).
- Sjostrand, T., Mrenna, S. & Skands, P. Z. A brief introduction to PYTHIA 8.1. *Comput. Phys. Commun.* **178**, 852–867 (2008).
- Burkert, A. The structure of dark matter halos in dwarf galaxies. *Astrophys. J. Lett.* **447**, L25–L28 (1995).
- Begeman, K. G., Broeils, A. H. & Sanders, R. H. Extended rotation curves of spiral galaxies: dark haloes and modified dynamics. *Mon. Not. R. Astron. Soc.* **249**, 523–537 (1991).

Acknowledgements

We thank A. Strong for his guidance in the implementation of the antinuclei propagation within the GALPROP code, A. Shukla and P. von Doetinchem for providing the ${}^3\text{He}$ production cross sections in cosmic-ray collisions with interstellar medium, and J. Herms and A. Ibarra for model calculations of the ${}^3\text{He}$ spectra stemming from DM annihilation. We would like to thank all the engineers and technicians for their invaluable contributions to the construction of the experiment

and the CERN accelerator teams for the outstanding performance of the LHC complex. We gratefully acknowledge the resources and support provided by all the grid centres and the Worldwide LHC Computing Grid (WLCG) collaboration. We acknowledge the following funding agencies for their support in building and running the ALICE detector: A. I. Alikhanyan National Science Laboratory (Yerevan Physics Institute) Foundation (ANSI), State Committee of Science and World Federation of Scientists (WFS), Armenia; Austrian Academy of Sciences, Austrian Science Fund (FWF): (M 2467-N36) and Nationalstiftung für Forschung, Technologie und Entwicklung, Austria; Ministry of Communications and High Technologies, National Nuclear Research Center, Azerbaijan; Conselho Nacional de Desenvolvimento Científico e Tecnológico (CNPq), Financiadora de Estudos e Projetos (Finep), Fundação de Amparo à Pesquisa do Estado de São Paulo (FAPESP), and Universidade Federal do Rio Grande do Sul (UFRGS), Brazil; Ministry of Education of China (MOEC), Ministry of Science & Technology of China (MSTC) and National Natural Science Foundation of China (NSFC), China; Ministry of Science and Education and Croatian Science Foundation, Croatia; Centro de Aplicaciones Tecnológicas y Desarrollo Nuclear (CEADEN), Cubaenergía, Cuba; Ministry of Education, Youth and Sports of the Czech Republic, Czech Republic; The Danish Council for Independent Research—Natural Sciences, the Villum Fonden, and Danish National Research Foundation (DNRF), Denmark; Helsinki Institute of Physics (HIP), Finland; Commissariat à l’Energie Atomique (CEA), Institut National de Physique Nucléaire et de Physique des Particules (IN2P3), and Centre National de la Recherche Scientifique (CNRS), France; Bundesministerium für Bildung und Forschung (BMBF) and GSI Helmholtzzentrum für Schwerionenforschung GmbH, Germany; General Secretariat for Research and Technology, Ministry of Education, Research and Religions, Greece; National Research, Development and Innovation Office, Hungary; Department of Atomic Energy Government of India (DAE), Department of Science and Technology, Government of India (DST), University Grants Commission, Government of India (UGC), and Council of Scientific and Industrial Research (CSIR), India; Indonesian Institute of Science, Indonesia; Istituto Nazionale di Fisica Nucleare (INFN), Italy; Japanese Ministry of Education, Culture, Sports, Science and Technology (MEXT) and Japan Society for the Promotion of Science (JSPS) KAKENHI, Japan; Consejo Nacional de Ciencia (CONACYT) y Tecnología, through Fondo de Cooperación Internacional en Ciencia y Tecnología (FONCICYT) and Dirección General de Asuntos del Personal Académico (DGAPA), Mexico; Nederlandse Organisatie voor Wetenschappelijk Onderzoek (NWO), Netherlands; The Research Council of Norway, Norway; Commission on Science and Technology for Sustainable Development in the South (COMSATS), Pakistan; Pontificia Universidad Católica del Perú, Peru; Ministry of Education and Science, National Science Centre and WUT ID-UB, Poland; Korea Institute of Science and Technology Information and National Research Foundation of Korea (NRF), Republic of Korea; Ministry of

Education and Scientific Research, Institute of Atomic Physics, Ministry of Research and Innovation and Institute of Atomic Physics, and University Politehnica of Bucharest, Romania; Joint Institute for Nuclear Research (JINR), Ministry of Education and Science of the Russian Federation, National Research Centre Kurchatov Institute, Russian Science Foundation and Russian Foundation for Basic Research, Russia; Ministry of Education, Science, Research and Sport of the Slovak Republic, Slovakia; National Research Foundation of South Africa, South Africa; Swedish Research Council (VR) and Knut & Alice Wallenberg Foundation (KAW), Sweden; European Organization for Nuclear Research, Switzerland; Suranaree University of Technology (SUT), National Science and Technology Development Agency (NSDTA), Suranaree University of Technology (SUT), Thailand Science Research and Innovation (TSRI), and National Science, Research and Innovation Fund (NSRF), Thailand; Turkish Energy, Nuclear and Mineral Research Agency (TENMAK), Turkey; National Academy of Sciences of Ukraine, Ukraine; Science and Technology Facilities Council (STFC), UK; National Science Foundation of the United States of America (NSF) and United States Department of Energy, Office of Nuclear Physics (DOE NP), USA. In addition, individual groups and members have received support from the German Research Foundation (DFG), Germany. The copyright of this Article is held by CERN, for the benefit of the ALICE Collaboration.

Author contributions

All authors contributed to the publication, being variously involved in the design and the construction of the detectors, in writing software, calibrating subsystems, operating the detectors and acquiring data, and finally analysing the processed data. The ALICE Collaboration members discussed and approved the scientific results. The manuscript was prepared by a subgroup of authors appointed by the collaboration and subject to an internal collaboration-wide review process. All authors reviewed and approved the final version of the manuscript.

Competing interests

The authors declare no competing interests.

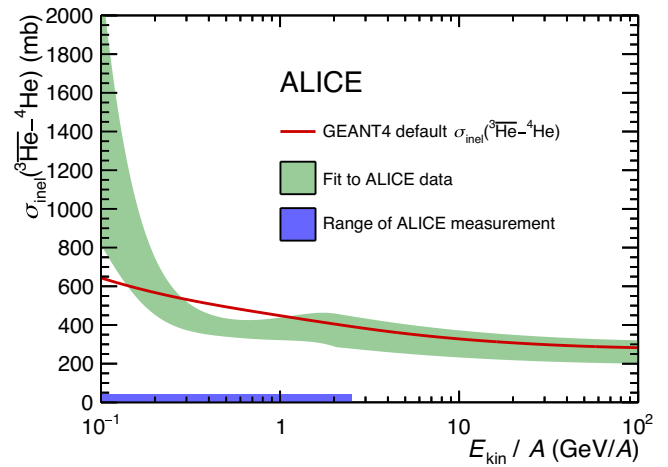
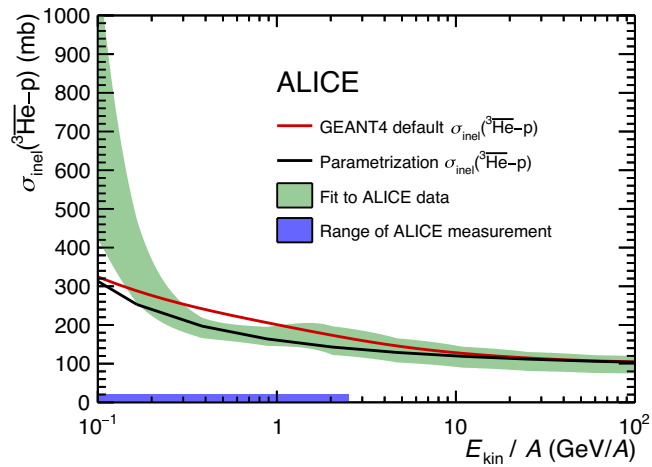
Additional information

Extended data is available for this paper at <https://doi.org/10.1038/s41567-022-01804-8>.

Correspondence and requests for materials should be addressed to alice-publications@cern.ch

Peer review information *Nature Physics* thanks the anonymous reviewers for their contribution to the peer review of this work

Reprints and permissions information is available at www.nature.com/reprints.



Extended Data Fig. 1 | Inelastic cross section for ^3He on protons and on ^4He . Inelastic cross section for ^3He on protons (left) and on ^4He (right). The green band shows the scaled ALICE measurement (see text for details), the red line represents the original GEANT 4 parametrization and the black line on the left

plot the parametrization employed in Ref. ³⁰. The width of the green band represents standard deviation uncertainty. The blue band on the x axis indicates the kinetic energy range corresponding to the ALICE measurement for $\sigma_{\text{inel}}(^3\text{He})$.